Turing instability and pattern formation in a two-population neuronal network model

John Wyller, Patrick Blomquist and Gaute T. Einevoll

Abstract

A two-population firing-rate model describing the dynamics of excitatory and inhibitory neural activity in one spatial dimension is investigated with respect to formation of patterns, in particular stationary periodic patterns and spatiotemporal oscillations. Conditions for existence of spatially homogeneous equilibrium states are first determined, and the stability properties of these equilibria are investigated. It is shown that the nonlocal synaptic interactions may promote a finite band-width instability in a way analogous to diffusion effects in the classical Turing instability for reaction-diffusion equations and modulational instability in the theory of nonlinear waves in nonlocal defocusing Kerr media. Our analysis relies on the wave-number dependent invariants of the 2×2-matrix representing the spatially Fourier-transformed linearized evolution equations. The generic picture which emerges is an instability consisting of a finite set of well-separated unstable bands in wave-number space (gain bands). The case with symmetric, exponentially decaying connectivity functions is investigated in detail, allowing for a more comprehensive analysis of the gain-band structure, and, in particular, conditions for the excitation of a single gain band through a Turing-Hopf bifurcation with the relative inhibition time constant as control parameter. Two typical situations emerge depending on the thresholds and inclinations of the sigmoidal firing-rate functions: (i) A single gain-band is excited through a Turing-Hopf bifurcation, and the resulting state is a spatiotemporally oscillating pattern, or (ii) the instability develops into a stationary periodic pattern, i.e., a set of equidistant bumps. The dependence of instability-type on the inclinations of the firing-rate function and the time constant are comprehensively investigated, demonstrating, for example, that only stationary patterns can be generated for sufficiently small inhibitory time constants. The nonlinear development of the gain-band instabilities is further elucidated by direct numerical simulations.

Key words: neural network, pattern formation, nonlocal, Turing instability

[1] E-mail: john.wyller@umb.no, patrick.blomquist@umb.no, gaute.einevoll@umb.no
[2] Address: Department of Mathematical Sciences and Technology and Center for Integrative Genetics, Norwegian University of Life Sciences, N-1432 Ås, Norway, Phone: +47-64965489, Fax: +47-64965401

1 Introduction

While mathematical descriptions of the salient features of signal processing in single neurons seem well established, the mathematical understanding of the signal-processing properties of biological neural networks is still meager [1]. Some successful network models connecting directly to experimental data have been developed for stimulus-driven responses, particularly in the early visual pathway (see, e.g., Ch. 2 in Ref. [1]). However, for the strongly interconnected cortical networks there are few such success stories. There are several reasons for this: the neurobiological properties of the circuit elements and their connections are less well mapped out, the neural activity is to a larger extent generated internally so that the noise-reducing procedure of stimulus-averaging is less useful [2], and the large number of synaptic connections makes the mathematical analysis of the models more difficult.

There is, however, a long tradition for studying simplified, firing-rate based cortical network models to investigate generic features such as the generation and/or stability of coherent structures such as stationary bumps (pulses) [3–13] or stationary periodic patterns [14–17], spatiotemporally oscillating patterns [9,18–21], or travelling waves, pulses and fronts [7,9,16,19,20,22–26]. Commonly, one (excitatory) [3] or two (excitatory+inhibitory) [27] neuronal populations in a single spatial dimension have been studied and modelled as a single or two coupled integro-differential equations describing the temporal change in neural activity of a particular neural element as a function of the sum of appropriately weighted synaptic inputs from neural activity in the entire network. In the simplest case the synaptic interactions are assumed to be instantaneous so that the dynamics essentially is determined by the time constants of the neural elements [3,27], but recent models have also incorporated finite action-potential propagation velocities [7,15,17,21]. For reviews of the comprehensive literature, see [2,28,29].

In the present work we investigate how various spatiotemporal and stationary spatial patterns are generated through Turing-type instabilities [14–21,30,31] in the following generic two-population model,

$$\begin{aligned}\partial_t u_\mathrm{e} = -u_\mathrm{e} &+ \int_{-\infty}^{\infty} \omega_\mathrm{ee}(x-x') P_\mathrm{e}(u_\mathrm{e}(x',t)-\theta_\mathrm{e})\,dx' \\ &- \int_{-\infty}^{\infty} \omega_\mathrm{ie}(x-x') P_\mathrm{i}(u_\mathrm{i}(x',t)-\theta_\mathrm{i})\,dx' \qquad (1a)\\ \tau\partial_t u_\mathrm{i} = -u_\mathrm{i} &+ \int_{-\infty}^{\infty} \omega_\mathrm{ei}(x-x') P_\mathrm{e}(u_\mathrm{e}(x',t)-\theta_\mathrm{e})\,dx' \\ &- \int_{-\infty}^{\infty} \omega_\mathrm{ii}(x-x') P_\mathrm{i}(u_\mathrm{i}(x',t)-\theta_\mathrm{i})\,dx' \,. \qquad (1b)\end{aligned}$$

Here $u_{\rm e}(x,t)$ and $u_{\rm i}(x,t)$ can be viewed as the somatic "activities" (e.g., membrane potentials) of an excitatory and an inhibitory neural element, respectively, at position x at time t [28]. $P_{\rm e}$ and $P_{\rm i}$ are non-negative functions, modelled as sigmoidal functions with parameterized maximum inclinations, converting the activity of these neural elements to firing rates with the parameters $\theta_{\rm e}$ and $\theta_{\rm i}$ adjusting the firing thresholds. The synaptic connectivity functions ω_{mn} $(m,n={\rm e,i})$ describe the coupling between the neural elements, and τ is the inhibitory time constant (measured relative to the excitatory time constant).

In a recent study we investigated the above model for the existence and stability of localized stationary solutions ('bumps') [13]. In the typical situation we observed that the stability of the bump solutions was lost through a Hopf-bifurcation when the inhibitory time constant increases beyond a critical value. Here we study a complementary aspect of the same model, namely the generation and formation of stationary periodic spatial patterns and spatiotemporal standing waves from a spatially homogeneous rest state through Turing-type instabilities.

Ermentrout and Cowan [14,18,19] (see also [28]) considered such instabilities in a more general setting for the analogous two-population Wilson-Cowan model [27] where the source terms on the right hand side of the equations in (1) are different; instead of a linear sum of sigmoidal-function inputs, sigmoidal functions are applied to the net sum of inputs [28]. A similar two-population model incorporating finite action-potential propagation times was considered by Laing and Coombes [21] where the stability of stationary and travelling waves were investigated under the assumption of Heaviside firing-rate functions using the Evans-function technique. It was demonstrated that the stability properties depend on the interplay between the time constants and the action-potential propagation speeds. Atay and Hutt [17] considered one-population models with finite propagation speeds for a large class of synaptic coupling functions, and found that the propagation speed had to be below a certain threshold value to generate spatiotemporal oscillations; for larger propagation speeds, i.e., smaller propagation delays, only stationary patterns could be generated.

In the present investigation of equation set (1) we consider various synaptic coupling functions ω_{mn} $(m,n={\rm e,i})$, but focus particularly on symmetric, exponentially decaying functions which allow for a detailed algebraic analysis of the pattern-forming features of the model. We further use sigmoidal firing-rate functions P_m $(m={\rm e,i})$ of varying inclinations. Our model implicitly assumes zero propagation delay. However, in contrast to the zero-delay finding in [17] for one-dimensional models, both stationary patterns and spatiotemporal oscillations can be generated by Turing-type instabilities by varying the threshold values and inclinations of the firing-rate functions. Here we investigate

and find conditions for the generation of both types of instability patterns and explore their parameter dependence.

The present methodology used to predict the so called gain-band structure relies on the wave-number dependent invariants of the 2×2-matrix representing the linearized, nonlocal dynamic equations for wave perturbations in spatial Fourier space. This procedure generalizes the stability techniques used in [14,18,20,32]. A prominent feature in this methodology is the possibility of detailing the instability structure, and in the present problem the generic picture which emerges is a finite band-width instability which consists of a set of well-separated gain bands. The number of such bands can be predicted from the number of transversal crossings of a parameterized curve in the invariant plane with the squared modulation wave number playing the role as parameter. Moreover, the technique can readily be used to predict processes of splitting, vanishing, excitation and coalescence of gain bands. The nonlinear development of the instability is detailed by means of numerical simulations, based on the XPPAUT-program developed by Ermentrout [33], demonstrating spatially or spatiotemporally periodic patterns as final outcomes of the instability mechanism.

The paper is organized as follows: In section 2 we formulate the model, and point out the general feature of boundedness of the solutions. Section 3 is devoted to the existence and uniqueness of spatial homogeneous equilibrium points, while section 4 analyses the stability of these points within the framework of the local limit of our model, i.e., the model that emerges when all the connectivity functions are approximated with Dirac δ-functions. In section 5 we describe the general theory for addressing the linear stability issue of the same equilibrium points for the full spatially nonlocal model. In section 6 the conditions for formation of gain bands is studied in detail for exponentially decaying synaptic connectivity functions. The Fourier spectrum for this type of connectivity function is positive definite, and the formation of a single gain band is the typical situation. We further consider an example with a rectangular connectivity function whose Fourier spectra are oscillating and are both positive and negative, and demonstrate how a multiple gain-band structure arises in this case. In section 7 numerical simulations are presented to illustrate our analytical findings and to study the nonlinear development of the detected instabilities. Further, we do a comprehensive study, for the case with exponentially decaying synaptic connectivity functions, of how the generation of the two types of instabilities vary with the properties of the firing-rate functions, in particular their inclinations, and the (relative) inhibitory time constant. Section 8 contains a brief summary and discussion. In Appendix A we present the general stability methodology underlying sections 5 and 6.

2 Model

We investigate a two-population model of the Wilson-Cowan type [13],

$$\partial_t u_{\mathrm{e}} = -u_{\mathrm{e}} + \omega_{\mathrm{ee}} * P_{\mathrm{e}}(u_{\mathrm{e}} - \theta_{\mathrm{e}}) - \omega_{\mathrm{ie}} * P_{\mathrm{i}}(u_{\mathrm{i}} - \theta_{\mathrm{i}}) \tag{2a}$$

$$\tau \partial_t u_{\mathrm{i}} = -u_{\mathrm{i}} + \omega_{\mathrm{ei}} * P_{\mathrm{e}}(u_{\mathrm{e}} - \theta_{\mathrm{e}}) - \omega_{\mathrm{ii}} * P_{\mathrm{i}}(u_{\mathrm{i}} - \theta_{\mathrm{i}}) \tag{2b}$$

for the time evolution of the activity level of the excitatory neural element ($u_{\mathrm{e}} = u_{\mathrm{e}}(x,t)$) and the inhibitory neural element ($u_{\mathrm{i}} = u_{\mathrm{i}}(x,t)$). The spatial domain is assumed to be infinite. Here $\omega_{mn} * f$ denotes the convolution integral defined by

$$(\omega_{mn} * f)(x) = \int_{-\infty}^{\infty} \omega_{mn}(y-x) f(y) dy, \quad m,n = \mathrm{e},\mathrm{i} \tag{3}$$

while ω_{mn} ($m,n = \mathrm{e},\mathrm{i}$) are *synaptic connectivity functions*, which are assumed to possess the following properties:

1. ω_{mn} is real-valued, positive and bounded, i.e.,

   $$0 \leq \omega_{mn}(x) \leq M$$

   for all $x \in \mathbb{R}$ and some constant $M > 0$.
2. ω_{mn} is symmetric, i.e.,

   $$\omega_{mn}(x) = \omega_{mn}(-x)$$

   for all $x \in \mathbb{R}$.
3. ω_{mn} is normalized, i.e.,

   $$\int_{-\infty}^{\infty} \omega_{mn}(x) dx = 1 \ .$$

4. The connectivity functions constitute a 1-parameter family of functions which can be written on the form

   $$\omega_{mn}(x) = \frac{1}{\sigma_{mn}} \cdot \Phi_{mn}(\xi_{mn}), \quad \xi_{mn} = \frac{x}{\sigma_{mn}} \tag{4}$$

   where the parameter σ_{mn} plays role as *synaptic footprint*.

Moreover, the functions P_m ($m = \mathrm{e},\mathrm{i}$) are the *firing-rate functions* for the excitatory ($m = \mathrm{e}$) and the inhibitory ($m = \mathrm{i}$) neural elements, respectively, satisfying the following properties:

1. The firing-rate functions P_m constitute a 1-parameter family of smooth, increasing functions for a finite parameter $\beta_m > 0$ measuring the inclination of the firing-rate functions.

2. The firing-rate functions define mappings from the set of real numbers to the unit interval, i.e.,
$$P_m : \mathbb{R} \to [0,1] \, .$$
3. The firing-rate functions approach the Heaviside function H in the distributional sense as $\beta_m \to \infty$.

The parameters θ_m represent threshold values for firing, which by assumption satisfy the requirement $0 < \theta_m \leq 1$ $(m = \mathrm{e}, \mathrm{i})$, while τ denotes the ratio between the inhibitory and excitatory time scales.

As examples of localized connectivity functions $\omega_{mn}(x) = \frac{1}{\sigma_{mn}} \cdot \Phi_{mn}(\xi_{mn})$, $\xi_{mn} = x/\sigma_{mn}$ satisfying our conditions we have the Gaussian

$$\Phi_{mn}(\xi_{mn}) = \frac{1}{\sqrt{\pi}} \exp(-\xi_{mn}^2) \, , \tag{5}$$

the exponentially decaying function

$$\Phi_{mn}(\xi_{mn}) = \frac{1}{2} \exp(-|\xi_{mn}|) \tag{6}$$

and the rectangular function

$$\Phi_{mn}(\xi_{mn}) = \begin{cases} \frac{1}{2}, & \text{if } -1 < \xi_{mn} < 1 \, ; \\ 0 & \text{otherwise} \end{cases} \tag{7}$$

while an example of a firing-rate function P_m is given by the sigmoidal function

$$P_m(u) = \frac{1}{2}(1 + \tanh(\beta_m u)) \, . \tag{8}$$

In the sequel we will assume that the firing-rate functions are modelled by (8).

From the properties of the connectivity functions ω_{mn} and the firing-rate functions P_m one deduces the bounds [13]

$$(V_\mathrm{e}(x) + 1)e^{-t} - 1 \leq u_\mathrm{e}(x,t) \leq (V_\mathrm{e}(x) - 1)e^{-t} + 1 \tag{9a}$$
$$(V_\mathrm{i}(x) + 1)e^{-t/\tau} - 1 \leq u_\mathrm{i}(x,t) \leq (V_\mathrm{i}(x) - 1)e^{-t/\tau} + 1 \tag{9b}$$

for the solutions. Here $(V_\mathrm{e}(x), V_\mathrm{i}(x))$ denotes the pair of initial conditions for the system (2). From this result we can draw the following conclusion: If the initial data satisfies $|V_m(x)| \leq 1 \, (m = \mathrm{e}, \mathrm{i})$ for all $x \in \mathbb{R}$, then $|u_m(x,t)| \leq 1$ for all $t \geq 0$. From the above discussion we can conclude that the compact subset $A \equiv \{u_m; |u_m| \leq 1\}$ of the state space plays the role as a global attractor set for the dynamical evolution prescribed by the model (2). Moreover, it proves that the nonlinear stage of the instabilities has to be saturated.

3 Existence and uniqueness of homogeneous equilibrium states

First we will consider the existence of a spatially homogeneous equilibrium of the system (2). We proceed as follows: The constant solutions of this system satisfy the coupled set of equations

$$u_{\mathrm{e}} = u_{\mathrm{i}} \tag{10a}$$

$$u_{\mathrm{e}} + P_{\mathrm{i}}(u_{\mathrm{i}} - \theta_{\mathrm{i}}) = P_{\mathrm{e}}(u_{\mathrm{e}} - \theta_{\mathrm{e}}) \; . \tag{10b}$$

The conditions imposed on the firing-rate functions P_m, i.e., that $0 < P_m(u) < 1$ for $|u| < \infty$, imply that possible equilibrium points must lie on the straight line $u_{\mathrm{e}} = u_{\mathrm{i}}$ subject to the constraint $-1 < u_m < 1$ $(m = \mathrm{e}, \mathrm{i})$, for all inclinations and threshold values used in the firing-rate functions. Thus the equilibrium points belong to the global attractor set for the model (2).

We here investigate existence and uniqueness of these equilibrium points. First let us address the existence issue. Notice that the system (10) can be translated into the problem

$$F(u_{\mathrm{e}}) \equiv u_{\mathrm{e}} + P_{\mathrm{i}}(u_{\mathrm{e}} - \theta_{\mathrm{i}}) - P_{\mathrm{e}}(u_{\mathrm{e}} - \theta_{\mathrm{e}}) = 0 \tag{11}$$

where $u_{\mathrm{e}} \in (-1, 1)$. Since $0 < P_m(u) < 1$ for all $|u| < \infty$, we find that $0 < F(1) < 2$ and $-2 < F(-1) < 0$ for all sets of parameters, and hence by appealing to the intermediate value theorem for continuous functions it is concluded that (11) has at least one solution $u_{\mathrm{e}} \equiv u_{\mathrm{eq}}$ in the interval $(-1, 1)$. Thus there always exists at least one homogeneous equilibrium $(u_{\mathrm{eq}}, u_{\mathrm{eq}})$ of the system (2). Notice that there is an *odd* number of transversal crossings $(F(u_{\mathrm{eq}}) = 0, F'(u_{\mathrm{eq}}) \neq 0)$, corresponding to an odd number of equilibrium points located on the line segment $u_{\mathrm{i}} = u_{\mathrm{e}}, -1 \leq u_m \leq 1$. The change in the number of equilibrium points is connected to the breakdown of the transversality condition, i.e., $F(u_{\mathrm{eq}}) = F'(u_{\mathrm{eq}}) = 0$, which imposes constraints on the parameters representing specific surfaces in the parameter space.

The next result relates to the number of zeros of the function F. Simple computation yields

$$F'(u_{\mathrm{e}}) = 1 + P_{\mathrm{i}}'(u_{\mathrm{e}} - \theta_{\mathrm{i}}) - P_{\mathrm{e}}'(u_{\mathrm{e}} - \theta_{\mathrm{e}}) \; . \tag{12}$$

Based on this expression we arrive at the following conclusions: First, since $0 < P_m'(u) \leq \frac{1}{2}\beta_m$ for all $|u| < \infty$, we deduce the bounds

$$1 - \frac{1}{2}\beta_{\mathrm{e}} < F'(u_{\mathrm{e}}) < 1 + \frac{1}{2}\beta_{\mathrm{i}}$$

on the derivative of F. This result together with the fact that $F(-1) < 0 < F(1)$, show that we get one and only one equilibrium point determined by

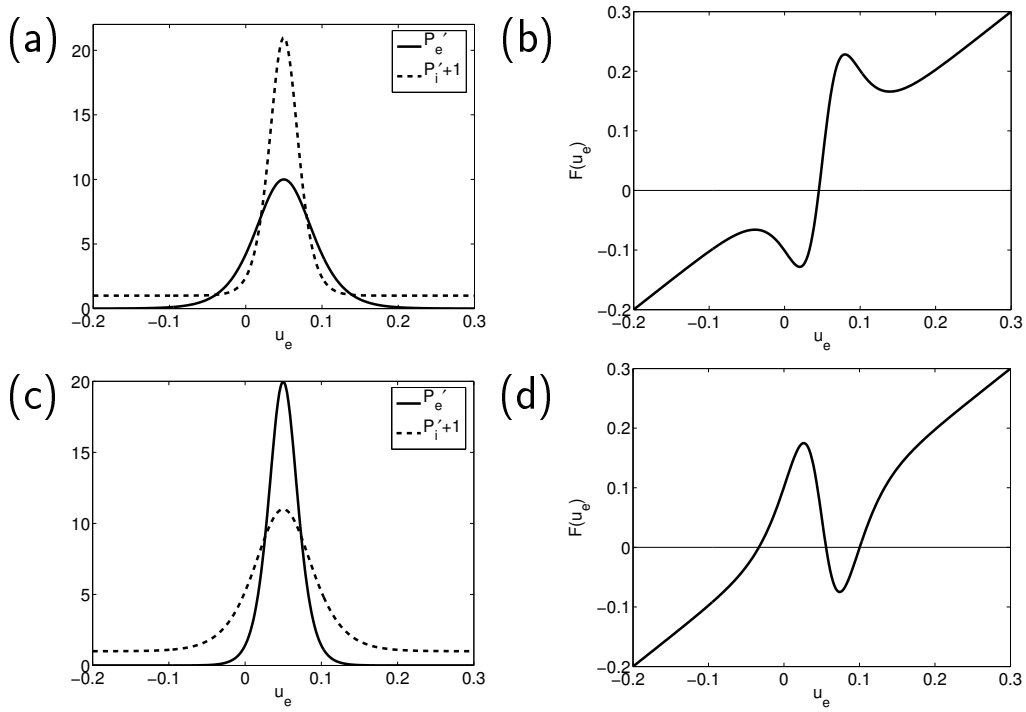


Fig. 1. Illustration of relationship between extremal points and equilibrium points. (a) For $\beta_{\rm e} < \beta_{\rm i} + 2$ the maximum number of extremal points and equilibrium points are four and five, respectively. Parameters: $\beta_{\rm e} = 20$, $\beta_{\rm i} = 40$ and $\theta_{\rm e} = \theta_{\rm i} = 0.05$. (b) $F(u_e)$ corresponding to a) with a single equilibrium point. (c) For $\beta_{\rm e} > \beta_{\rm i} + 2$ the maximum number of extremal points and equilibrium points are two and three, respectively. Parameters: $\beta_{\rm e} = 40$, $\beta_{\rm i} = 20$ and $\theta_{\rm e} = \theta_{\rm i} = 0.05$. (d) $F(u_e)$ corresponding to c) with three equilibrium points.

(10) if $\beta_{\rm e} < 2$. The expression for $F'(u_{\rm e})$ also shows that this result can be extended to include the endpoint $\beta_{\rm e} = 2$.

Secondly, the properties of the derivative of F enable us to estimate the maximum number of equilibrium points in different parameter regimes. We observe that the functions $1 + P_{\rm i}'(u_{\rm e} - \theta_{\rm i})$ and $P_{\rm e}'(u_{\rm e} - \theta_{\rm e})$ are symmetric with respect to the threshold values $\theta_{\rm e}$ and $\theta_{\rm i}$, respectively. Moreover, the maximum amplitude of these functions are $1 + \frac{1}{2}\beta_{\rm i}$ and $\frac{1}{2}\beta_{\rm e}$, respectively. Finally the typical widths of these two functions are inversely proportional to $\beta_{\rm i}$ and $\beta_{\rm e}$. The solution of the equation $1 + P_{\rm i}'(u_{\rm e} - \theta_{\rm i}) = P_{\rm e}'(u_{\rm e} - \theta_{\rm e})$ yields the extremal points of F. A careful analysis now reveals that the maximum number of extremal points is four provided $\beta_{\rm e} < \beta_{\rm i} + 2$, while in the complementary regime ($\beta_{\rm e} > \beta_{\rm i} + 2$) we always have exactly two extremal points. This result together with the fact that $F(-1) < 0 < F(1)$, imply that the maximum number of equilibrium points is five (three) if $\beta_{\rm e} < \beta_{\rm i} + 2$ ($\beta_{\rm e} > \beta_{\rm i} + 2$). Notice that the situation with five equilibrium points can only occur for $\theta_{\rm e}$ close to $\theta_{\rm i}$ and $\beta_{\rm e} < \beta_{\rm i} + 2$, due to the fact that only this situation may produce four extremal points. The graphs of the functions $1 + P_{\rm i}'(u_{\rm e} - \theta_{\rm i})$ and $P_{\rm e}'(u_{\rm e} - \theta_{\rm e})$ as well as corresponding

Table 1
Properties of two parameter sets, labelled A and B, chosen in the present firing-rate functions $P_m(m = \mathrm{e}, \mathrm{i})$ in (8). The corresponding single equilibrium points $(u_{\mathrm{eq}}, u_{\mathrm{eq}})$ for the spatially homogeneous system, P'_{e} and P'_{i} (15), τ_{H} (17), and $\tau_{\pm}$ (18) are also listed.

	β_{e}	β_{i}	θ_{e}	θ_{i}	u_{eq}	P'_{e}	P'_{i}	τ_{H}	τ_-	τ_+
Parameter set A	20	30	0.10	0.12	0.129	7.26	13.94	2.39	1.36	4.20
Parameter set B	5	10	0.05	0.10	0.106	2.31	4.98	4.56	1.27	16.35

plots of the function $F(u_{\mathrm{e}})$ are shown in Fig. 1 for the two example parameter sets.

4 Linear stability theory in local limit

Let us assume that all the synaptic widths approach zero. This means that our normalized connectivity functions approach the Dirac delta function, i.e., $\omega_{mn}(x) \to \delta(x)$. Then (2) is reduced to a 2D autonomous dynamical system,

$$\partial_t u_{\mathrm{e}} = -u_{\mathrm{e}} + P_{\mathrm{e}}(u_{\mathrm{e}} - \theta_{\mathrm{e}}) - P_{\mathrm{i}}(u_{\mathrm{i}} - \theta_{\mathrm{i}}) \tag{13a}$$
$$\tau \partial_t u_{\mathrm{i}} = -u_{\mathrm{i}} + P_{\mathrm{e}}(u_{\mathrm{e}} - \theta_{\mathrm{e}}) - P_{\mathrm{i}}(u_{\mathrm{i}} - \theta_{\mathrm{i}}) \tag{13b}$$

which means that the process is homogeneous with respect to space. One notices that the local system (13) indeed possesses the same equilibrium points as the full nonlocal model (10).

The stability of these equilibrium points is analyzed by means of standard techniques for autonomous dynamical systems: The Jacobian $\mathbf{J}$ of the system (13) evaluated at the equilibrium points is given as

$$\mathbf{J} = \begin{bmatrix} -1 + P'_{\mathrm{e}} & -P'_{\mathrm{i}} \\ \tau^{-1} P'_{\mathrm{e}} & -\tau^{-1}(1 + P'_{\mathrm{i}}) \end{bmatrix} \tag{14}$$

where P'_m is defined as

$$P'_m \equiv \left. \frac{dP_m(v)}{dv} \right|_{v = u_{m,\mathrm{eq}} - \theta_m} = \beta_m \, sech^2\Big(\beta_m(u_{m,\mathrm{eq}} - \theta_m)\Big)/2, \quad m = \mathrm{e}, \mathrm{i}\,. \tag{15}$$

Due to the scaling property $P'_m \sim \beta_m$, we will refer to the positive parameters $P'_m\,(m = \mathrm{e}, \mathrm{i})$ as the *inclination* parameters of the firing-rate functions P_m. In Fig. 2 we show the firing-rate functions P_{e} and P_{i} in situations with large and small values of the inclination parameters β_m (cf. Table 1). We will focus on

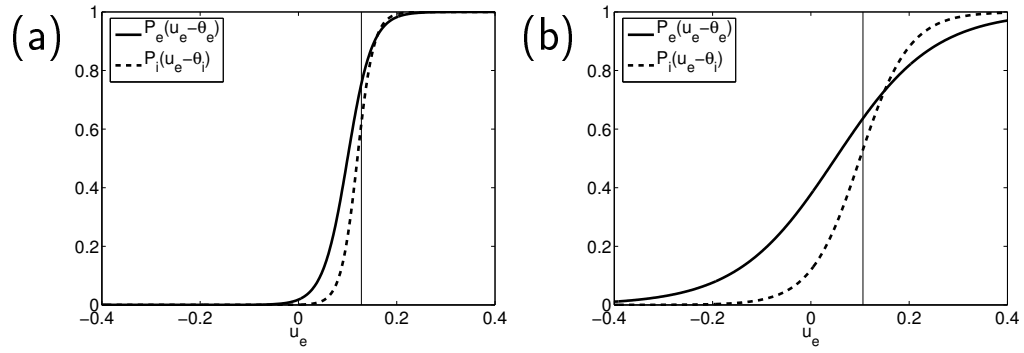


Fig. 2. Illustration of firing-rate functions P_e and P_i defined by (8) and the location of the homogeneous equilibrium u_eq (vertical lines) determined by (11) for (a) parameter set A and (b) parameter set B, cf. Table 1. The slope of the graphs of P_e and P_i at the equilibrium point yields the inclination parameters P_e' and P_i' given by (15).

these two sets of parameter values, denoted 'parameter set A' and 'parameter set B', respectively, in the analysis and numerical examples below.

The stability of the equilibria can now be investigated in a standard way solely by means of the invariants of the Jacobian $\mathbf{J}$, i.e., the trace and the determinant which are given as

$$det(\mathbf{J}) = \tau^{-1}(P_\mathrm{i}' - P_\mathrm{e}' + 1) = \tau^{-1}F'(u_\mathrm{eq}) \tag{16a}$$

$$tr(\mathbf{J}) = P_\mathrm{e}' - 1 - \frac{1}{\tau}(1 + P_\mathrm{i}') = (P_\mathrm{e}' - 1)(1 - \frac{\tau_\mathrm{H}}{\tau}) \tag{16b}$$

where F is given by (11), and τ_H is defined by

$$\tau_\mathrm{H} \equiv \frac{P_\mathrm{i}' + 1}{P_\mathrm{e}' - 1}\,. \tag{17}$$

Notice that τ_H may assume both positive and negative values. For $P_\mathrm{e}' > 1$ we will refer to τ_H as the Hopf time.

The linear stability properties of the local problem are determined by the relative inhibition time τ and the inclination parameters P_m' $(m = \mathrm{e}, \mathrm{i})$ of the firing-rate functions. The result is outlined below.

4.1 Saddle-point situation

When $F'(u_\mathrm{eq}) < 0$, the two eigenvalues of (14) are real and have opposite signs for all values of τ, which means that the equilibrium is a saddle point. From the analysis presented in the previous section it is concluded that the saddle-point situation only can occur in the multiple-equilibrium situation, i.e., when the

system (2) has more than one equilibrium point. Notice also that a necessary (but not sufficient) condition for having a saddle-point situation is $P'_{\rm e} > 1$.

4.2 Node-focus situation

If $F'(u_{\rm eq}) > 0$, we have either a node or a focus. Moreover, simple computation reveals that the discriminant Δ_{loc} of the eigenvalue equation is given as

$$\begin{aligned}\Delta_{loc} &= \tau^{-2}(p_2 - 2p_1\tau + p_0\tau^2)\\ p_2 &= (P'_{\rm i} + 1)^2\\ p_1 &= F'(u_{\rm eq}) + P'_{\rm i}P'_{\rm e}\\ p_0 &= (P'_{\rm e} - 1)^2\end{aligned}$$

from which it follows that for all choices of $(P'_{\rm e}, P'_{\rm i})$ there are distinct positive values of τ denoted by $\tau_\pm$ for which the discriminant changes sign. The actual values are given as

$$\tau_\pm \equiv \frac{(\sqrt{F'(u_{\rm eq})} \pm \sqrt{P'_{\rm e}P'_{\rm i}})^2}{(P'_{\rm e} - 1)^2}\ . \tag{18}$$

Notice that $\tau_- \to (P'_{\rm i}+1)^2/2P'_{\rm i}$ and $\tau_+ \to +\infty$ as $P'_{\rm e} \to 1$. We conclude that for $0 \le \tau \le \tau_-$ or $\tau \ge \tau_+$ $(P'_{\rm e} \neq 1)$, we have a node, while in the complementary regime we get a focus.

Finally, if $P'_{\rm e} \le 1$, then $tr(\mathbf{J}) < 0$ and $det(\mathbf{J}) > 0$ for all τ, and hence we have stability for all τ values. In the complementary regime $(P'_{\rm e} > 1)$ the stability depends on the relative inhibition time. From the sign of $tr(\mathbf{J})$, one finds stability (instability) for $\tau < \tau_{\rm H}$ $(\tau > \tau_{\rm H})$.

4.3 Hopf-bifurcation. Poincaré-Bendixsons theorem

Assume $P'_e > 1$ and $F'(u_{\rm eq}) > 0$ so that we are in a node-focus situation. The critical value $\tau_{\rm H}$ corresponds to a Hopf bifurcation point. The outcome of this bifurcation is according to standard theory the excitation of a limit cycle. The limit cycle behavior can in fact be extended to the whole range $\tau > \tau_{\rm H}$ provided there is a unique equilibrium. This equilibrium must be an unstable node or focus since we in this case must have $F'(u_{\rm eq}) > 0$. Let C denote the boundary of the square $-1 < u_m < 1$ in the phase plane and $\underline{F}$ the vector field

$$\underline{F}(u_{\rm e}, u_{\rm i}) = [-u_{\rm e} + P_{\rm e}(u_{\rm e} - \theta_{\rm e}) - P_{\rm i}(u_{\rm i} - \theta_{\rm i}), \tau^{-1}(-u_{\rm i} + P_{\rm e}(u_{\rm e} - \theta_{\rm e}) - P_{\rm i}(u_{\rm i} - \theta_{\rm i})]^T$$

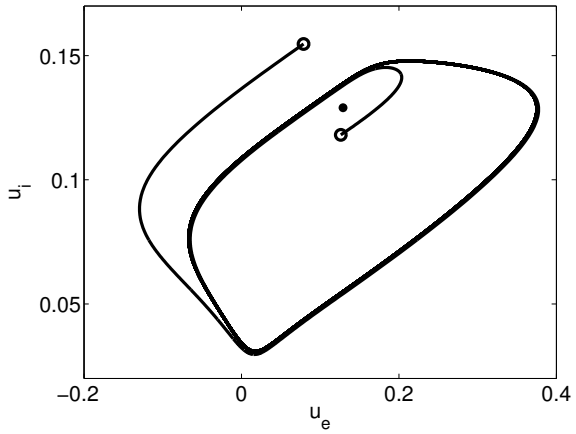


Fig. 3. Limit cycle for values of τ greater than the Hopf bifurcation point for parameter set A in Table 1 ($\tau = 5 > \tau_{\mathrm{H}} = 2.39$). The dot corresponds to the equilibrium point, while the circles represent two different initial conditions. Generated with XPPAUT [33].

defining the local system (13). By exploiting the fact that $0 < P_m(u) < 1 (m = \mathrm{e}, \mathrm{i})$ for $|u| < \infty$ we find that $\underline{F} \cdot \underline{n} < 0$ on C. Here $\underline{n}$ denotes the outwards unit normal to C. Then, by appealing to Poincaré-Bendixsons theorem (see for example [34]), we conclude that there is at least one limit cycle in the trapping set $-1 < u_m < 1$ for all $\tau > \tau_{\mathrm{H}}$ in the node-focus case (i.e., when $F'(u_{\mathrm{eq}}) > 0$) enclosing this equilibrium point. Fig. 3 illustrates this property.

Finally, let us investigate a multiple-equilibrium situation consisting of three equilibrium points corresponding to the solutions of the system (13), which by previous results turns out to represent the most typical multiple-equilibrium scenario. These points are identified with points $u_{\mathrm{eq},i}$ of the function $F(u_{\mathrm{e}})$ which we conveniently put in the order $-1 < u_{\mathrm{eq},1} < u_{\mathrm{eq},2} < u_{\mathrm{eq},3} < 1$. These zero points alternate between having a positive and a negative derivative: $F'(u_{\mathrm{eq},i}) > 0$ $(i = 1, 3)$, $F'(u_{\mathrm{eq},2}) < 0$. The zero point $u_{\mathrm{eq},2}$ correspond to a saddle point, while the two other zero points $u_{\mathrm{eq},i}$ $(i = 1, 3)$ correspond to foci or nodes. The set $-1 < u_m < 1$ is also in this case a trapping set. In Fig. 4 we illustrate the typical features of the phase plane when $u_{\mathrm{eq},i}$ $(i = 1, 3)$ are unstable foci. Notice that the multiple equilibrium situation as described here occurs if the three equilibrium points are located in the range for which the firing-rate functions are steep ($P_e' > 1$).

In the next sections we will focus on the effect of spatial nonlocality on the stability properties of the equilibrium points defined by (11).

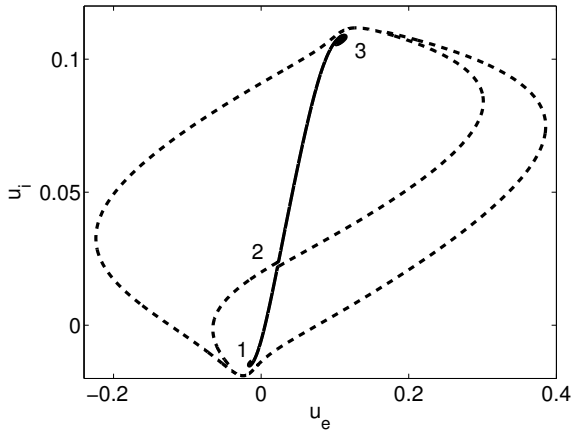


Fig. 4. Stable manifolds (solid curves) and unstable manifolds (dashed curves) of the saddle point (no. 2). The stable manifolds have the two other equilibrium points (no. 1 and no. 3) as source. The model parameters are $\beta_{\rm e} = 28.513$, $\beta_{\rm i} = 20.333$, $\theta_{\rm e} = 0.0489$, $\theta_{\rm i} = 0.0633$, $\tau = 6.85$. The Hopf bifurcation points for equilibrium points no. 1 and no. 3 are $\tau_{\rm H,1} = 5.56$ and $\tau_{\rm H,3} = 6.83$, respectively. The points no. 1 and no. 3 are foci. Generated with XPPAUT [33].

5 Stability problem for full model: General theory

We start out by linearizing the coupled set of equations (2) about the spatial homogeneous equilibrium of the model, i.e., the solutions $(u_{\rm e}, u_{\rm i}) = (u_{\rm eq}, u_{\rm eq}) \equiv \underline{u}_{\rm eq}, -1 < u_{\rm eq} < 1$ of the equilibrium equations (10), by inserting the ansatz

$$u_{\rm e}(x,t) = u_{\rm eq} + \phi(x,t), \quad u_{\rm i}(x,t) = u_{\rm eq} + \psi(x,t) \tag{19}$$

where ϕ and ψ are small perturbations imposed on the constant background described by $(u_{\rm eq}, u_{\rm eq})$ ($|\phi|, |\psi| \ll |u_{\rm eq}|$), and linearize the resulting equations. Doing this we end up with the linearized system of nonlocal evolution equations

$$\partial_t \phi = -\phi + P'_{\rm e}\, \omega_{\rm ee} * \phi - P'_{\rm i}\, \omega_{\rm ie} * \psi \tag{20a}$$
$$\tau \partial_t \psi = -\psi + P'_{\rm e}\, \omega_{\rm ei} * \phi - P'_{\rm i}\, \omega_{\rm ii} * \psi\ . \tag{20b}$$

The next step consists of converting the system (20) to a set of ordinary differential equations by using the Fourier technique. We deduce the system

$$\partial_t \hat{\phi} = -\hat{\phi} + P'_{\rm e}\hat{\omega}_{\rm ee}\hat{\phi} - P'_{\rm i}\hat{\omega}_{\rm ie}\hat{\psi}$$
$$\tau \partial_t \hat{\psi} = -\hat{\psi} + P'_{\rm e}\hat{\omega}_{\rm ei}\hat{\phi} - P'_{\rm i}\hat{\omega}_{\rm ii}\hat{\psi}$$

by means of

$$\hat{\omega}_{mn}(k) \equiv \int_{-\infty}^{\infty} \omega_{mn}(x) \exp(ikx) dx \tag{21a}$$

$$\hat{\phi}(k,t) \equiv \int_{-\infty}^{\infty} \phi(x,t) \exp(ikx) dx \tag{21b}$$

$$\hat{\psi}(k,t) \equiv \int_{-\infty}^{\infty} \psi(x,t) \exp(ikx) dx \tag{21c}$$

and the convolution theorem for Fourier transforms. Notice that the Fourier transforms are real-valued, even functions of k. This system can be conveniently rewritten on matrix form as

$$\partial_t \underline{X} = \mathbf{A} \cdot \underline{X} \tag{22}$$

where $\mathbf{A}$ and $\underline{X}$ are defined as

$$\mathbf{A} = \begin{bmatrix} P_{\mathrm{e}}' \hat{\omega}_{\mathrm{ee}} - 1 & -P_{\mathrm{i}}' \hat{\omega}_{\mathrm{ie}} \\ \tau^{-1} P_{\mathrm{e}}' \hat{\omega}_{\mathrm{ei}} & -\tau^{-1}(P_{\mathrm{i}}' \hat{\omega}_{\mathrm{ii}} + 1) \end{bmatrix} , \tag{23}$$

$$\underline{X} = [\hat{\phi}, \hat{\psi}]^T . \tag{24}$$

The invariants of the coefficient matrix $\mathbf{A}$ can now be computed as

$$det(\mathbf{A}) = \tau^{-1}((1 + P_{\mathrm{i}}' \hat{\omega}_{\mathrm{ii}})(1 - P_{\mathrm{e}}' \hat{\omega}_{\mathrm{ee}}) + P_{\mathrm{e}}' P_{\mathrm{i}}' \hat{\omega}_{\mathrm{ie}} \hat{\omega}_{\mathrm{ei}}) \tag{25a}$$

$$tr(\mathbf{A}) = P_{\mathrm{e}}' \hat{\omega}_{\mathrm{ee}} - 1 - \tau^{-1}(P_{\mathrm{i}}' \hat{\omega}_{\mathrm{ii}} + 1) . \tag{25b}$$

(In passing we note that these invariants have the same structure as the expressions 8.12 and 8.13 in [28] for the Wilson-Cowan model [27], but the model parameters and their interpretations are somewhat different.)

We always have two modes in the problem corresponding to the two eigenvalues λ_+ and λ_- given by

$$\lambda_{\pm} = \frac{1}{2}\Big(tr(\mathbf{A}) \pm \sqrt{(tr(\mathbf{A}))^2 - 4 det(\mathbf{A})} \Big) . \tag{26}$$

The mode corresponding to λ_+ (λ_-) is referred to as the $\lambda_+(\lambda_-)$-*mode*. Notice also that since $\hat{\omega}_{mn}(k) = \hat{\omega}_{mn}(-k)$, we have $\lambda_{\pm}(k) = \lambda_{\pm}(-k)$. Hence the variation of the eigenvalues with the wave number k can be expressed in terms of the squared wave number $\eta = k^2$. Now, since the differential equations (22)-(24) constitute a 2D linear autonomous system with constant coefficients, we can exploit the invariants of the coefficient matrix $\mathbf{A}$ to determine the stability properties: Each $\eta = k^2$ corresponds to a point in the $tr(\mathbf{A}), det(\mathbf{A})$-plane (which we refer to as the *invariant plane*). Thus, when letting η vary continuously from 0 to $+\infty$, a parameterized curve $\underline{\gamma}$ defined as

$$\underline{\gamma}(\eta) = (tr(\mathbf{A})(\eta), det(\mathbf{A})(\eta)), \quad \eta \geq 0 \tag{27}$$

is traced out in the invariant plane. This means that we can study the stability problem in a simple geometrical way: We have stability if the curve $\underline{\gamma}$ remains in the second quadrant for all $\eta \geq 0$, while an instability occurs if there is an η-interval for which the curve is outside this quadrant. An η-interval producing an instability is referred to as a *gain band*. The gain bands caused by the λ_+ (λ_-)-mode are consequently termed $\lambda_+(\lambda_-)$ gain bands. Moreover, the number of transversal crossings of the $tr(\mathbf{A})$-axis and the positive $det(\mathbf{A})$-axis in the invariant plane determines the number of gain bands excited.

A detailed account of this stability methodology is given in Appendix A for a general 2×2 system.

5.1 Short-wavelength limit

Since the connectivity functions satisfy the normalization condition, Riemann-Lebesque lemma implies that the Fourier transforms $\hat{\omega}_{mn}$ $(m, n = \mathrm{e}, \mathrm{i})$ are continuous functions of k and $\lim_{|k|\to\infty} \hat{\omega}_{mn}(k) = 0$. Hence we have

$$\mathbf{A} \sim \begin{bmatrix} -1 & 0 \\ 0 & -\tau^{-1} \end{bmatrix}$$

as $k \to +\infty$ from which it follows that

$$\begin{aligned} det(\mathbf{A}) &= \tau^{-1} > 0 \\ tr(\mathbf{A}) &= -1 - \tau^{-1} < 0 \end{aligned}$$

in this asymptotic limit. Hence the curve $\underline{\gamma}$ will enter the second quadrant in the invariant plane, regardless of the particular shape of the connectivity functions. This means that *any instability must if it exists be of the finite bandwidth type regardless of the particular shape of the connectivity functions.*

5.2 Smooth spectra of connectivity functions

Next, let us assume the functions $x\omega_{mn}(x)$ to be absolute integrable. Then, since by assumption $\omega_{mn}(x)$ is positive and even, it follows that

$$\int_{-\infty}^{\infty} x\omega_{mn}(x)dx = 0; \quad m, n = \mathrm{e}, \mathrm{i}$$

for this class of connectivity functions. Riemann-Lebesque lemma now implies that the derivatives $\hat{\omega}'_{mn}(k)$ are the Fourier transforms of the functions

$x\omega_{mn}(x)$. Moreover, $\hat{\omega}'_{mn}(k)$ are continuous functions and satisfy $\lim_{|k|\to\infty}\hat{\omega}'_{mn}(k) = 0$. In that case the curve $\underline{\gamma}$ is a smooth curve, and the general picture of the linear stage of the instability that emerges is a finite set of well-separated gain bands.

5.3 Long-wavelength limit

In the long-wavelength limit we have

$$det(\mathbf{A})(k=0) = \tau^{-1}(1 + P'_{\mathrm{i}} - P'_{\mathrm{e}}) = \tau^{-1}F'(u_{\mathrm{eq}}) \tag{28a}$$

$$tr(\mathbf{A})(k=0) = P'_{\mathrm{e}} - 1 - \tau^{-1}(P'_{\mathrm{i}} + 1) = (P'_{\mathrm{e}} - 1)(1 - \frac{\tau_{\mathrm{H}}}{\tau}) \tag{28b}$$

since by the definition of the Fourier transform (21) and the normalization condition imposed on the connectivity functions ω_{mn}, we have $\hat{\omega}_{mn}(0) = 1$. Here $F(u_{\mathrm{eq}})$ and τ_{H} are defined by means of (11) and (17), respectively. Notice also that (28) coincides with the local limit (16). Hence in the long-wavelength limit the theory elaborated for the local limit is directly applicable, and, due to continuity, the features described for $k = 0$ must also hold true for some k-interval symmetrically centered about $k = 0$. We conclude that a sufficient condition for having instability is that either $det(\mathbf{A}) < 0$ or $tr(\mathbf{A}) > 0$ for $k = 0$. From the expressions (28) we see that these conditions are translated into (i) $F'(u_{\mathrm{eq}}) < 0$ or (ii) $P'_{\mathrm{e}} > 1$ and $\tau > \tau_{\mathrm{H}}$, respectively. Note that this type of long-wavelength instability ($k \to 0$) is independent of the type of connectivity functions chosen.

5.4 Gain-band formation

A necessary but not sufficient condition to have stability is that the trajectory $\underline{\gamma}$ starts out in the second quadrant of the invariant plane. In this case the stability properties depend sensitively on the type of connectivity functions chosen. Further, possible instabilities are presented as a set of well-separated gain bands for non-zero wave numbers.

Asymptotic stability requires that $det(\mathbf{A}) > 0$ and $tr(\mathbf{A}) < 0$ for all k. The expression (25a) shows that $det(\mathbf{A})$ is positive for all k provided the conditions

1. $P'_{\mathrm{e}}\hat{\omega}_{\mathrm{ee}}(k_{\mathrm{max}}) \leq 1$
2. $\hat{\omega}_{\mathrm{ii}}(k) > 0$
3. $\hat{\omega}_{\mathrm{ei}}(k)\hat{\omega}_{\mathrm{ie}}(k) > 0$

are satisfied. Here $\hat{\omega}_{\mathrm{ee}}(k_{max})$ denotes the maximum value of the spectrum $\hat{\omega}_{\mathrm{ee}}$.

Notice that the first condition is satisfied for $P_e' \leq 1$ and $\hat{\omega}_{ee}(k) \leq 1$. The requirement, $\hat{\omega}_{ee}(k) \leq 1$, is satisfied for ω_{ee} being exponentially decaying, gaussian or rectangular. The two remaining conditions are satisfied for connectivity functions ω_{ii}, ω_{ei} and ω_{ie} possessing positive definite spectra, e.g., exponentially decaying or gaussian.

Let us now investigate the sign of $tr(\mathbf{A})$. If the connectivity functions ω_{ee} and ω_{ii} satisfy the conditions 1. and 2. above, we conclude from (25b) that $tr(\mathbf{A}) < 0$, and hence the trajectory $\underline{\gamma}$ remains in the second quadrant in the invariant plane. As an example, a set of positive definite spectra $\hat{\omega}_{mn}$ where $\hat{\omega}_{ee}(k) \leq 1$, will produce stable situations for all τ provided $P_e' \leq 1$.

This analysis clearly reveals that in order to look for scenarios which produce finite band-width instabilities, a natural approach is to search in regimes where at least one of the conditions listed above ceases to be valid. For example, if the spectra of the connectivity functions are positive definite with the extra constraint $\hat{\omega}_{ee}(k) \leq 1$, one should search in the inclination regime $P_e' > 1$. Another possibility consists of choosing connectivity functions for which at least one of the spectra is not sign definite. We will pursue these problems below.

As shown in Appendix A formation and coalescence of gain bands are connected to nontransversal crossings of the $tr(\mathbf{A})$-axis and the positive $det(\mathbf{A})$-axis in the invariant plane of the trajectory $\underline{\gamma}$ defined by (25) and (27). These types of crossings indicate that bifurcation phenomena take place. The special case characterized by a wave number k_H for which we locally have (i) $det(\mathbf{A})(\eta_H = k_H^2) > 0$ and $tr(\mathbf{A})(\eta_H = k_H^2) = 0$, and (ii) $tr(\mathbf{A}) < 0$ for $\eta \neq \eta_H$ (i.e. a non-transversal crossing at $\eta = \eta_H$), is referred to as a *Turing-Hopf bifurcation* [20]. In analogy with the procedure detailed in [20] a Hopf normal form of the system (2) can be derived for the approximate behavior of the dynamics in the vicinity of the Hopf point. Based on this normal form one can show that a breather or a travelling wave is excited. Moreover, conditions for having stable breathers and travelling waves can be expressed in terms of the coefficients of the normal form. We do not pursue the derivation of the normal form coefficients here, however.

6 Stability problem for full model: Case studies

In this section we demonstrate concrete examples on (i) existence and excitation of a gain band for the case with (positive definite) exponentially decaying connectivity function, (ii) conditions for exciting a gain band through a Turing-Hopf bifurcation for this system and (iii) the formation of multiple gain bands in the case of rectangular connectivity functions possessing not

sign definite spectra.

6.1 Gain-band formation for exponentially decaying connectivity functions

Let us model the connectivity functions (4) by means of exponentially decaying functions (6). In this case the Fourier transform is given as the Lorentzian

$$\hat{\omega}_{mn}(\eta) = \frac{1}{1+\sigma_{mn}^2\eta}, \quad \eta = k^2, \quad m,n = \mathrm{e},\mathrm{i} \tag{29}$$

and the determinant and trace of the coefficient matrix are given as

$$det(\mathbf{A}) = \tau^{-1}\frac{H_4(\eta)}{(1+\sigma_{\mathrm{ee}}^2\eta)(1+\sigma_{\mathrm{ii}}^2\eta)(1+\sigma_{\mathrm{ei}}^2\eta)(1+\sigma_{\mathrm{ie}}^2\eta)} \tag{30a}$$

$$tr(\mathbf{A}) = \frac{Q_2(\eta)}{(1+\sigma_{\mathrm{ee}}^2\eta)(1+\sigma_{\mathrm{ii}}^2\eta)} \; . \tag{30b}$$

Here Q_2 is the quadratic polynomial defined by

$$Q_2(\eta) = q_2\eta^2 + q_1\eta + q_0 \tag{31}$$

with the coefficients $q_i, i = 0,1,2$, given as

$$q_2 = -(1+\frac{1}{\tau})\sigma_{\mathrm{ee}}^2\sigma_{\mathrm{ii}}^2 \tag{32a}$$

$$q_1 = (P_{\mathrm{e}}'-1)\sigma_{\mathrm{ii}}^2 - \sigma_{\mathrm{ee}}^2 - \frac{1}{\tau}((P_{\mathrm{i}}'+1)\sigma_{\mathrm{ee}}^2 + \sigma_{\mathrm{ii}}^2) \tag{32b}$$

$$q_0 = P_{\mathrm{e}}' - 1 - \frac{1}{\tau}(1+P_{\mathrm{i}}') = (P_{\mathrm{e}}'-1)(1-\frac{\tau_{\mathrm{H}}}{\tau}) \tag{32c}$$

and H_4 is the quartic polynomial

$$H_4(\eta) = h_4\eta^4 + h_3\eta^3 + h_2\eta^2 + h_1\eta + h_0 \; . \tag{33}$$

Here $h_0 = F'(u_{\mathrm{eq}})$ while the remaining coefficients (listed in Appendix B) are given as cumbersome algebraic expressions with the notable feature that $h_4 > 0$. We assume that the equilibrium state is node or focus within the framework of the local model ($F'(u_{\mathrm{eq}}) > 0$), which implies that $h_0 > 0$. In the following we also assume that $P_{\mathrm{e}}' > 1$ and $\tau < \tau_{\mathrm{H}}$, so that $q_0 < 0$ which according to previously obtained results means that stability is assured in the long-wavelength limit, i.e., $det(\mathbf{A})(\eta = 0) > 0$, $tr(\mathbf{A})(\eta = 0) < 0$.

We first notice that the maximum number of $\lambda_\pm$ gain bands is three. This result follows from the fact that the maximum number of positive zeros of Q_2 and

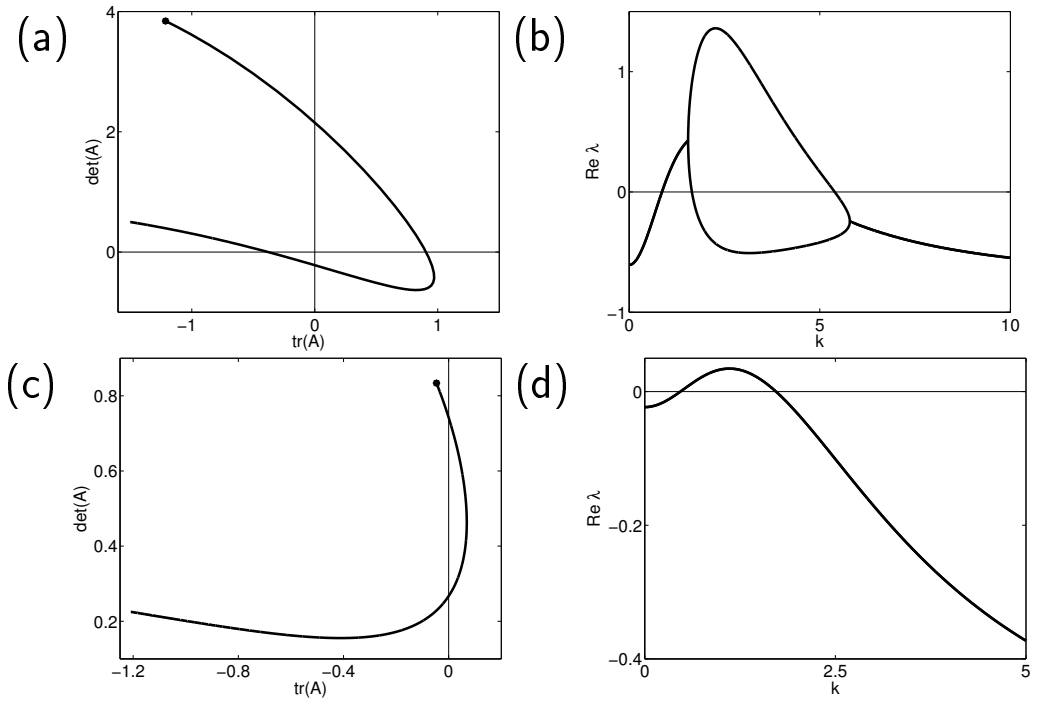


Fig. 5. Examples of single gain-band situations for exponentially decaying connectivity functions (6). Synaptic footprints are $\sigma_{ee} = 0.35$, $\sigma_{ei} = 0.48$, $\sigma_{ie} = 0.60$ and $\sigma_{ii} = 0.69$. In (a) the parameterized curve $\underline{\gamma}$ in the invariant plane defined by means of (25) and (27) is shown for $\tau = 2$ for the firing-rate function corresponding to parameter set A with $\tau_H = 2.39$ (cf. Table 1). In (b) the corresponding growth rates ($Re\lambda$ in (26)) are shown as a function of wave number. In (c) a corresponding curve $\underline{\gamma}$ are shown for $\tau = 4.4$ with parameter set B (cf. Table 1) where $\tau_H = 4.56$, for the same synaptic footprints. The corresponding growth rates are shown in (d); the presence of only a single curve implies that the two eigenvalues are complex conjugate in the entire interval of k-values. The black dots in (a) and (c) denote the starting points of the curves, $\eta = k^2 = 0$.

H_4 is two and four, respectively. The complexity of the quartic polynomial H_4 prevents us from inferring simple analytical predictions regarding the crossings of the $tr(\mathbf{A})$-axis. We generally thus have to rely on numerical computations to explore the details of the gain-band structure.

In Fig. 5a a single unstable-band situation is demonstrated for the parameter set A in the case of exponentially decaying synaptic connectivity functions. These firing-function parameters as well as τ are chosen to comply with the condition $P_e' > 1$ and $\tau < \tau_H$ to assure stability in the long-wavelength limit (see Table 1). As seen in the panel, the trajectory $\underline{\gamma}$ starts and ends in the second quadrant but passes through the other three quadrants. The real part of the corresponding eigenvalues (cf. (26)) is shown in Fig. 5b illustrating that the real part of one or both eigenvalues is positive unless the trajectory $\underline{\gamma}$ is in the second quadrant.

6.2 Conditions for Turing-Hopf bifurcations

We now investigate conditions for generating a single gain band through a Turing-Hopf bifurcation. We focus on the situation where the model parameters are chosen such that $H_4(\eta) > 0$, i.e., $det(\mathbf{A}) > 0$, for all η. In order to detect a Turing-Hopf bifurcation we study the properties of $tr(\mathbf{A})$, i.e., $Q_2(\eta)$. From (31)-(32c) we immediately see that $tr(\mathbf{A})$ is independent of the synaptic cross-coupling footprints σ_{ei} and σ_{ie}. Thus the single gain-band generation is in this case governed only by σ_{ee}, σ_{ii}, P'_{e}, P'_{i}, and τ. Elementary analysis shows that Q_2 has two strictly positive zeros denoted by η_+ and η_- ($\eta_+ > \eta_-$) if the discriminant $\Delta_{Q_2} \equiv q_1^2 - 4q_0q_2$ is strictly positive and $q_1 > 0$. Both these conditions can be translated into conditions for these parameters.

We here consider the relative inhibition time τ to be a control parameter, and a value of τ producing coalescence of two positive zeros (i.e., $\eta_+ = \eta_-$) represents a Turing-Hopf bifurcation. The latter situation occurs when $Q_2(\eta_\pm) = Q'_2(\eta_\pm) = 0$, which by elementary analysis means that $\Delta_{Q_2} = 0$ for some positive value of the relative inhibition time τ.

With this background we can now elaborate on the conditions for getting a gain band through a Turing-Hopf bifurcation. We start out by observing that Q_2 has a global maximum at

$$\eta = \eta_{\mathrm{c}} \equiv -\frac{q_1}{2q_2} \, . \tag{34}$$

In order to get crossings with the $det(\mathbf{A})$-axis we must restrict the study to situations where Q_2 possesses a positive maximum point. The expression (34) shows that $\eta_{\mathrm{c}} > 0$ if and only if $q_1 > 0$ (since $q_2 < 0$). From the expression for q_1 we find that the relative inhibition time τ must satisfy

$$\tau > \tau_{\mathrm{c}}, \quad \tau_{\mathrm{c}} \equiv \frac{P'_{\mathrm{i}} + 1 + \frac{\sigma_{\mathrm{ii}}^2}{\sigma_{\mathrm{ee}}^2}}{(P'_{\mathrm{e}} - 1)\frac{\sigma_{\mathrm{ii}}^2}{\sigma_{\mathrm{ee}}^2} - 1} \, . \tag{35}$$

Moreover, in order to have the initial point of the curve $\underline{\gamma}$ in the second quadrant we must have

$$\tau_{\mathrm{c}} < \tau_{\mathrm{H}} \tag{36}$$

where τ_{H} is given by means of (17). Notice that for $\tau_{\mathrm{c}} > 0$ the condition (36) is equivalent to the condition

$$\frac{\sigma_{\mathrm{ii}}^2}{\sigma_{\mathrm{ee}}^2} > \tau_{\mathrm{H}} \frac{P'_{\mathrm{e}}}{P'_{\mathrm{i}}} = \frac{P'_{\mathrm{i}} + 1}{P'_{\mathrm{i}}} \cdot \frac{P'_{\mathrm{e}}}{P'_{\mathrm{e}} - 1} \tag{37}$$

on the ratio between the synaptic widths σ_{ii} and σ_{ee}. Thus we immediately see that only models with $\sigma_{\mathrm{ii}} > \sigma_{\mathrm{ee}}$ may give a Turing-Hopf bifurcation.

We now explore conditions for obtaining $\Delta_{Q_2} = 0$. Simple computation shows that Δ_{Q_2} can be expressed as

$$\Delta_{Q_2} = \tau^{-2}\vartheta_2(\tau), \quad \vartheta_2(\tau) \equiv f_2\tau^2 + f_1\tau + f_0 \tag{38}$$

where the coefficients $f_i, i = 0, 1, 2$, of the quadratic polynomial ϑ_2 in τ are given as

$$f_2 = \sigma_{\mathrm{ee}}^4(1 - \frac{\sigma_{\mathrm{ii}}^2}{\sigma_{\mathrm{ee}}^2} + P_e'\frac{\sigma_{\mathrm{ii}}^2}{\sigma_{\mathrm{ee}}^2})^2 \tag{39a}$$

$$f_1 = -2\sigma_{\mathrm{ee}}^4(P_{\mathrm{e}}' - 1)(\frac{\sigma_{\mathrm{ii}}^2}{\sigma_{\mathrm{ee}}^2} - \Omega_-)(\frac{\sigma_{\mathrm{ii}}^2}{\sigma_{\mathrm{ee}}^2} - \Omega_+) \tag{39b}$$

$$f_0 = \sigma_{\mathrm{ee}}^4(1 - \frac{\sigma_{\mathrm{ii}}^2}{\sigma_{\mathrm{ee}}^2} + P_{\mathrm{i}}')^2 \ . \tag{39c}$$

Here

$$\Omega_\pm = \frac{-F'(u_{\mathrm{eq}}) - P_{\mathrm{e}}'P_{\mathrm{i}}' - 1 \pm \sqrt{(F'(u_{\mathrm{eq}}) + P_{\mathrm{e}}'P_{\mathrm{i}}' + 1)^2 + 4(P_{\mathrm{e}}' - 1)(P_{\mathrm{i}}' + 1)}}{2(P_{\mathrm{e}}' - 1)} \tag{40}$$

and we find that $\Omega_- < 0 < \Omega_+$ in our regime where $P_{\mathrm{e}}' > 1$.

We search for positive values of τ for which $\Delta_{Q_2} = 0$, and a first requirement is that the discriminant $\Delta_{\vartheta_2} \equiv f_1^2 - 4f_0f_2$ of the polynomial ϑ_2 is nonnegative. This discriminant is found to be

$$\Delta_{\vartheta_2} = 16\sigma_{\mathrm{ii}}^2\sigma_{\mathrm{ee}}^2P_{\mathrm{i}}'P_{\mathrm{e}}'(\sigma_{\mathrm{ii}}^2 - \sigma_{\mathrm{ee}}^2)(\sigma_{\mathrm{ee}}^2(P_{\mathrm{i}}' + 1) + \sigma_{\mathrm{ii}}^2(P_{\mathrm{e}}' - 1)) \tag{41}$$

and we thus see that Δ_{ϑ_2} automatically is positive when the constraint (37) is fulfilled (since it implies $\sigma_{\mathrm{ii}} > \sigma_{\mathrm{ee}}$).

Since $f_0, f_2 > 0$ we must have $f_1 < 0$ to be in the position to have $\Delta_{Q_2} = 0$ for positive values of τ. From (39b) we thus have the new constraint $\sigma_{\mathrm{ii}}^2/\sigma_{\mathrm{ee}}^2 > \Omega_+$ which apparently comes in addition to the constraint (37) on the synaptic widths. However, it can be shown that $\Omega_+ < \tau_{\mathrm{H}}P_{\mathrm{e}}'/P_{\mathrm{i}}'$ so that the new constraint will be fulfilled if (37) is fulfilled.

The expression for ϑ_2 (with $f_1 < 0$) shows that the discriminant Δ_{Q_2} may change sign for two positive values of τ which we denote by $\tilde{\tau}_\pm$. With (37) fulfilled, the ordering of τ_{c}, τ_{H} and $\tilde{\tau}_\pm$ gives the final conclusions with respect to the possibility of having a Turing-Hopf bifurcation. We first exclude the possibility that both zeros of ϑ_2 are located outside the range $\tau_{\mathrm{c}} < \tau < \tau_{\mathrm{H}}$ since this eventually implies a strictly negative discriminant Δ_{Q_2}. Next, by continuously deforming the graph of Q_2 (using τ as deformation parameter) from $\tau = \tau_{\mathrm{c}}$ to $\tau = \tau_{\mathrm{H}}$ we conclude that there is a single τ-value producing a

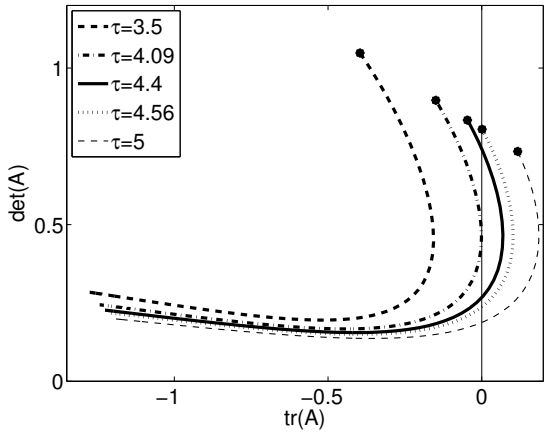


Fig. 6. Generation of a single unstable gain band by varying the relative inhibition time τ in the case of exponentially decaying synaptic connectivity functions for parameter set B (cf. Table 1). Synaptic footprints as in Fig. 5. The Turing-Hopf relative inhibition time is found to be about 4.09 by the non-transversality condition $tr(\mathbf{A}) = \frac{d}{d\eta} tr(\mathbf{A}) = 0$. The black dots denote the starting point of the curves $\eta = k^2 = 0$.

nontransversal crossing. Since ϑ_2 has two zeros, only one of them can belong to the range $\tau_c < \tau < \tau_H$. Thus only the orderings $\tau_c < \tilde{\tau}_- < \tau_H < \tilde{\tau}_+$ and $\tilde{\tau}_- < \tau_c < \tilde{\tau}_+ < \tau_H$ represent situations where a gain band is excited at a unique value for the relative inhibition time, $\tilde{\tau}_-$ or $\tilde{\tau}_+$, through a Turing-Hopf bifurcation. We will then have at least one gain band for a range of relative inhibition times, $\tilde{\tau}_+(\tilde{\tau}_-) < \tau < \tau_H$.

In Figs. 5c and 5d a gain band resulting from such a Turing-Hopf situation is demonstrated for the parameter set B listed in Table 1. As seen in Fig. 5c, $det(\mathbf{A}) > 0$ for the entire trajectory, and a gain band is excited when the trajectory passes into the first quadrant ($tr(\mathbf{A}) > 0$). For this parameter set $\tau_H = 4.56$ (cf. Table 1), and τ is set to 4.4 in the example so that the constraint $\tau < \tau_H$ is fulfilled. Further, $\tau_H P'_e / P'_i = 2.12$, and since $(\sigma_{ii}/\sigma_{ee})^2 = 3.89$, the constraint (37) is also fulfilled. We further find $\tilde{\tau}_- = 0.03$, $\tilde{\tau}_+ = 4.09$, and $\tau_c = 2.41$. We are thus in the situation where $\tilde{\tau}_- < \tau_c < \tilde{\tau}_+ < \tau < \tau_H$ where, according to the description above, a gain band is excited.

The eigenvalues (26) corresponding to the parameterized curve $\underline{\gamma}$ in Figs. 5c are complex conjugate for the part of the curve visiting the first quadrant in the invariant plane, since for this range of wave numbers $(tr(\mathbf{A}))^2 < 4det(\mathbf{A})$. The corresponding gain curve i.e., the real part of the eigenvalues as a function of the wave number k is displayed in Fig. 5d. Hence each unstable mode in the band exhibits temporal oscillations. The frequency of the oscillations is given by the imaginary part of the eigenvalues. On the contrary, the gain-band structure seen in Fig. 5 for parameter set A is somewhat more complicated in the sense that only a portion of the gain band yields complex eigenvalues

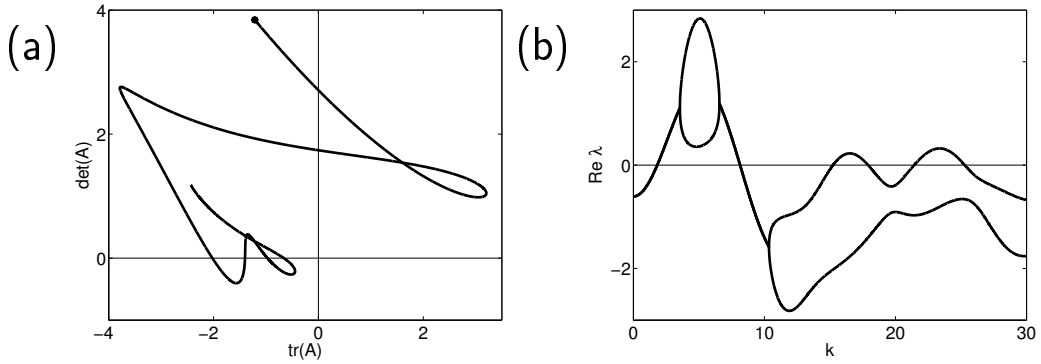


Fig. 7. Example of a multiple gain-band situation with synaptic connectivity functions given as rectangular functions (7) in for the parameter set A (cf. Table 1) and the same synaptic footprints as in Fig. 5. (a) Parameterized curve $\underline{\gamma}$ in the invariant plane defined by means of (25) and (27). (b) Corresponding growth rate ($Re\lambda$ in (26)).

and thus modes oscillating in time (Fig. 5b). This can be inferred from the behavior of the parameterized curve $\underline{\gamma}$ in the invariant plane in Fig. 5a. In this case the quartic polynomial H_4 is not sign definite but has two zeros.

Further, in Fig. 6 we demonstrate how the gain band in Fig. 5c may be interpreted as stemming from a Turing-Hopf bifurcation (using the same model parameters as in Fig. 5b, except for τ which is now a control parameter). In the figure we see that the trajectory remains in the second quadrant of the invariant plane for $\tau < \tilde{\tau}_+ = 4.09$, passes into the first quadrant for a finite value of the wave number for $\tilde{\tau}_+ = 4.09 < \tau < \tau_{\rm H} = 4.56$, while the homogeneous background state becomes unstable for $\tau > \tau_{\rm H} = 4.56$. We thus have a Turing-Hopf bifurcation point at $\tau = \tilde{\tau}_+ = 4.09$, and a gain band is excited for $\tilde{\tau}_+ < \tau < \tau_{\rm H}$, i.e., $4.09 < \tau < 4.56$.

Note that the gain-band structure in Fig. 5a, corresponding to the parameter set A, cannot stem from a Turing-Hopf bifurcation with τ as control parameter. In Fig. 5a the trajectory $\underline{\gamma}$ is seen to pass into the lower half plane ($det(\mathbf{A}) < 0$). Since the sign of $det(\mathbf{A})$ is independent of τ (cf. (25a)), there will thus be a gain-band excited for all values of τ.

6.3 Multiple gain-band structure

In order to easily obtain an example of gain-band structure with multiple unstable gain bands we choose a connectivity function whose Fourier spectra oscillates in k-space. A typical example of such a connectivity function is given by the rectangular connectivity function (7) whose Fourier transform is given

by

$$\hat{\omega}_{mn}(k) = \frac{\sin(k\sigma_{mn})}{k\sigma_{mn}} \; . \tag{42}$$

In Fig. 7a the existence of three unstable gain bands is demonstrated in the invariant plane. Fig. 7b shows the corresponding growth rates. An analysis of the curve $\underline{\gamma}$ reveals that the number of transversal crossings with the coordinate axes in this plane can be used to predict the number of gain bands (cf. Appendix A).

7 Numerical simulations

In this section we illustrate some of the results in the previous sections with direct simulations of (2). In particular, we focus on (i) how the linear instabilities described by the gain-band structure manifest themselves in numerical simulations with the homogeneous background state plus an added disturbance as initial condition, (ii) how the instabilities develop beyond the linear regime, and (iii) how the type of instability, i.e., generating either purely spatial or spatiotemporal oscillations, depends on the properties of the firing-rate functions.

In the numerical simulations we consider a finite spatial domain, $-5 \leq x \leq 5$, with periodic boundary conditions. A spatial grid with a spacing of $\Delta x = 0.05$ is used, and our models can thus be viewed as a network model with 201 excitatory and 201 inhibitory neurons on a ring. We used the program XPPAUT, developed by Ermentrout [33], with Runge-Kutta R4 with $dt = 0.01$ as integration method.

We employed the same sets of firing-rate parameters and synaptic connectivity functions as in the case studies in Sec. 6. The initial condition was a low-amplitude narrow rectangular box of neural activity superimposed on the homogeneous background given by the equilibrium points in Table 1. The narrow rectangular box contains a wide spectrum of spatial frequencies so that the various gain bands can be excited.

We follow the exposition in the previous section and first focus on the two examples with exponentially decaying connectivity functions in Fig. 5 for which a single gain band exist. Then we consider the multiple gain-band example with rectangular connectivity functions in Fig. 7.

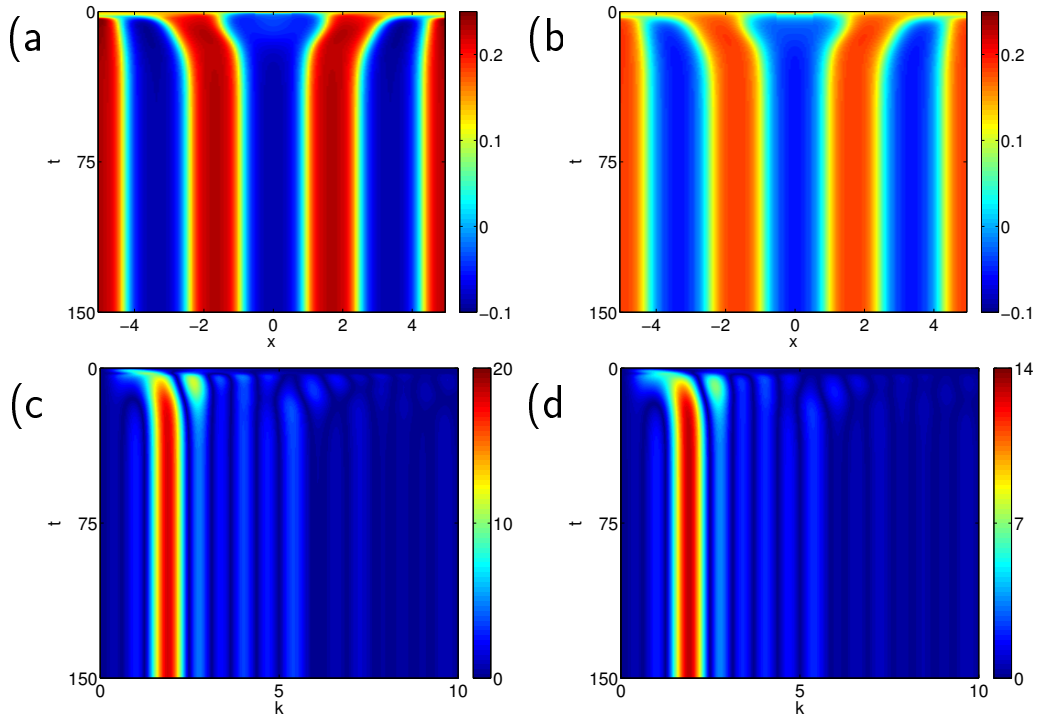


Fig. 8. Dynamical evolution for parameter set A investigated in Figs. 5a and 5b from an initial state consisting of a homogeneous background state ($u_e = u_i = 0.129$, cf. Table 1) with a narrow centered rectangular box superimposed ($-0.5 < x < 0.5$, $u_e = u_i = 0.2$). (a) Excitatory activity level, $u_e(x,t)$. (b) Inhibitory activity level, $u_i(x,t)$. In (c) and (d) the Fourier spectra of (a) and (b), respectively, are shown.

7.1 Parameter set A: Demonstration of spatial oscillations

We first consider the example in Fig. 5a, corresponding to parameter set A. In Figs. 8a and 8b the dynamical evolution of the neural activity u_e and u_i is shown. For the chosen value of τ ($\tau = 2$) the theory in the previous section predicts a gain-band instability, and we see that the instability develops into a purely, spatial periodic pattern. In Fig. 5b we observe that the wave number k of the fastest growing mode (maximum $Re\lambda$) is approximately 2. The Fourier spectra of the spatial patterns as a function of time depicted in Figs. 8c and 8d show that after a short initial phase the resulting spatial pattern is dominated by wave numbers of about 2 as well. Thus in the initial phase energy leaks into the fastest growing mode ($k \approx 2$) which turns out to be stable.

A notable feature is that the stationary pattern consists of periodically distributed bumps. Each bump resembles the single stationary bumps studied by us in [13] in a model with gaussian connectivity functions and infinitely steep firing-rate functions (Heaviside unit step functions). In Fig. 9 we show a single stationary bump obtained with the same exponentially decaying connectivity functions as in Fig. 5 but with Heaviside firing-rate functions, using the same

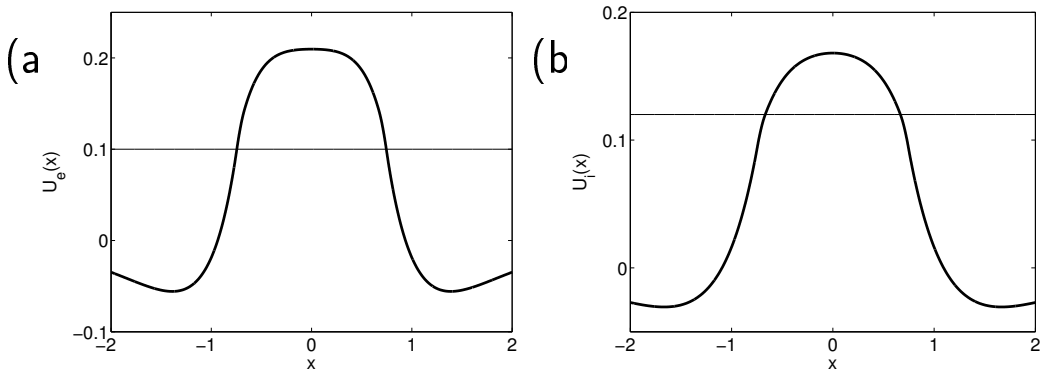


Fig. 9. Spatially oscillating structure found for exponentially decaying connectivity functions with the same synaptic footprints and relative time constant as in Fig. 8. Firing-rate functions are given as a Heaviside functions, i.e., $P_m(U_m) = H(U_m - \theta_m)$ $(m = \mathrm{e}, \mathrm{i})$ where $\theta_\mathrm{e} = 0.1$ and $\theta_\mathrm{i} = 0.12$ (horizontal lines). (a) Excitatory activity level $U_\mathrm{e}(x)$ (cf. Fig. 1 in [13]). (b) Corresponding inhibitory activity level $U_\mathrm{i}(x)$.

method as described in [13]. Comparison with Figs. 8a and 8b shows that this bump, both in terms of shape and size, is similar to one of the bumps in the spatially oscillating pattern found for parameter set A, for which the values of the inclination parameters β_e and β_i are large (cf. Table 1). This suggests that the dynamics predicted by the firing-rate functions for large values of the inclination parameters effectively mimic the dynamics corresponding to the Heaviside functions.

7.2 Parameter set B: Demonstration of spatiotemporal oscillations

The dynamical evolution corresponding to Figs. 5c and 5d (i.e., parameter set B) is shown in Figs. 10a and 10b. Here we see that the instability develops into spatiotemporal oscillations. This is consistent with the phase described by two complex conjugate eigenvalues of the coefficient matrix $\mathbf{A}$, where the frequency of the oscillations is given by the imaginary part of the eigenvalues. In Fig. 5d we observe that the wave number k of the fastest growing mode (maximum $Re\lambda$) is approximately 1. The Fourier spectra of the spatial patterns as a function of time depicted in Fig. 10c and 10d show that after a short initial phase the resulting spatial pattern is dominated by wave numbers of about 1 as well. Thus as for parameter set A energy leaks into the fastest growing mode ($k \approx 1$).

7.3 Relationship between inclination parameters and pattern formation

The different instability patterns observed for the parameter sets A and B describing firing-rate functions motivates an inquiry into what aspects of the

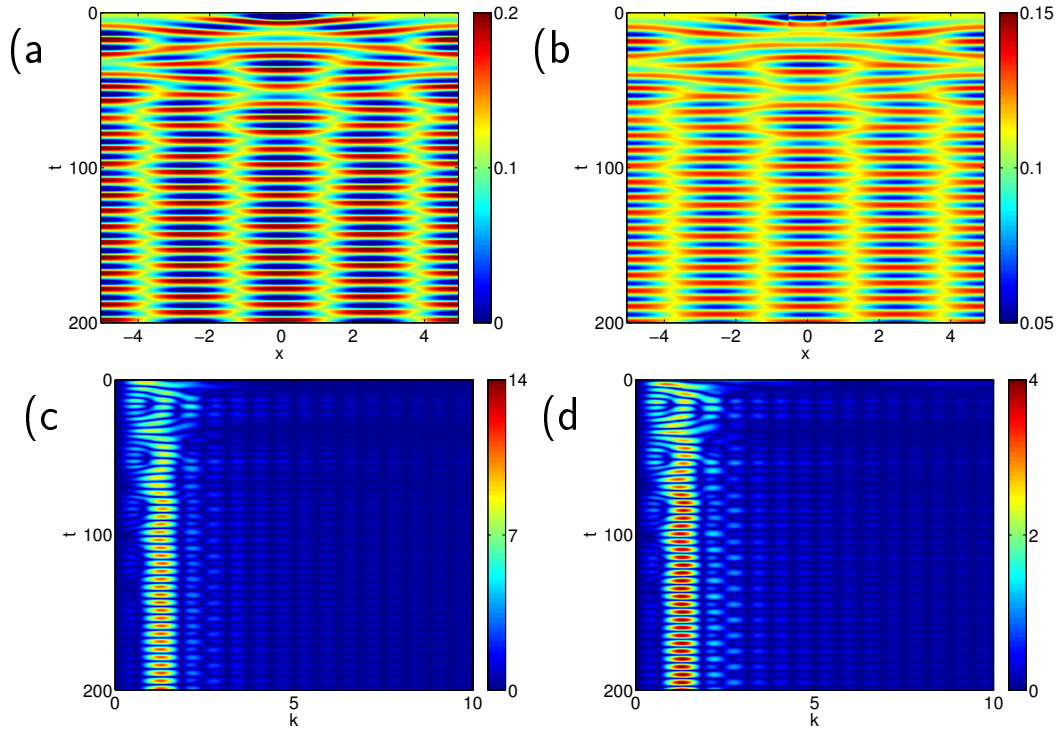


Fig. 10. Dynamical evolution covered in Fig. 5c and 5d from an initial state consisting of a homogeneous background state ($u_\mathrm{e} = u_\mathrm{i} = 0.106$, cf. Table 1) with a narrow centered rectangular box superimposed ($-0.5 < x < 0.5$, $u_\mathrm{e} = u_\mathrm{i} = 0.2$) for parameter set B. (a) Excitatory activity level, $u_\mathrm{e}(x,t)$. (b) Inhibitory activity level, $u_\mathrm{i}(x,t)$. In (c) and (d) the Fourier spectra (a) and (b), respectively, are shown.

rate functions causes the qualitatively different behavior. Inspection of Table 1 shows that parameter set A has significantly larger values for the inclination parameters β_e and β_i, compared to parameter set B. We thus investigate the pattern formation as a function of β_m ($m = \mathrm{e}, \mathrm{i}$) in more detail and pursue this as follows: We first determine the number of equilibrium points of the local system (13) for a dense array of inclination parameters β_m ($m = \mathrm{e}, \mathrm{i}$) for two sets of threshold values, $\theta_\mathrm{e} = 0.1, \theta_\mathrm{i} = 0.12$ (from parameter set A) and $\theta_\mathrm{e} = 0.05, \theta_\mathrm{i} = 0.1$ (from parameter set B). We then consider the same synaptic footprints as in Fig. 5 and systematically evaluate the dynamical outcome of the linear instability for each point in the array covering the $(\beta_\mathrm{e}, \beta_\mathrm{i})$-plane, for both sets of threshold values. We further consider two choices for the inhibitory time constant: (i) τ slightly smaller than the local Hopf time τ_H (for the particular values of $\beta_\mathrm{e}, \beta_\mathrm{i}, \theta_\mathrm{e}, \theta_\mathrm{i}$) given by (17), i.e., $\tau = \tau_\mathrm{H} - 0.07$, and (ii) a low τ-regime ($\tau = 0.001$) corresponding to nearly instantaneously reacting inhibitory neurons.

The results from this analysis are given by the color plots in Fig. 11, and several features become evident: For $\theta_\mathrm{e} = 0.1, \theta_\mathrm{i} = 0.12$ in Fig. 11a regions corresponding both to the generation of stationary spatial patterns

and to generation of spatiotemporal oscillations are prevalent. For example, while $\beta_e = 20, \beta_i = 30$, corresponding to parameter set A, generates a stationary pattern, $\beta_e = 5, \beta_i = 30$ generates spatiotemporal oscillations. For $\theta_e = 0.05, \theta_i = 0.1$ in Fig. 11b the generation of stationary spatial oscillations appears to be very rare (in the situation with a single local equilibrium). Only a tiny region in the inclination-parameter plane around $\beta_e = 4, \beta_i = 2$ generates such stationary patterns.

For $\tau \to 0$ ($\tau = 0.001$, Fig. 11c-d) we see that the regions corresponding to generation of spatiotemporal oscillations in Fig. 11c-d have vanished, i.e., no spatiotemporal oscillations can be formed, at least from a situation with a single local equilibrium. This can be understood by direct inspection of (25): for sufficiently small τ, $tr(\mathbf{A})$ will always be strictly negative, and a Turing-Hopf instability generating spatiotemporal oscillations cannot occur. The region corresponding to generation of stationary spatial patterns is the same as for the larger values of τ (cf. Fig. 11a-b). This can also be understood by inspection of (25) since the sign of $det(\mathbf{A})$, determining the generation of such patterns, is seen to be independent of τ. For $\theta_e = 0.05, \theta_i = 0.1$ in Fig. 11d we thus find that patterns can be only be formed in a tiny region in the inclination-parameter plane around $\beta_e = 4, \beta_i = 2$.

Notice that the finding of a lack of generation of spatiotemporal oscillations for very small τ appears to be consistent with the results from Atay and Hutt [17]. They considered a general one-population model and found that only stationary spatial patterns could be generated for models with no action-potential propagation delay. For $\tau = 0$, our model (2) can essentially be reduced to a one-population model (with no action-potential propagation delay) [4], and the same observation as in [17] is made (cf. Fig. 11c-d).

7.4 Multiple gain bands

In Fig. 12 we show the dynamical development of the model with rectangular connectivity functions exhibiting multiple gain-band instability (cf. Fig. 7). The initial condition is as before a narrow rectangular box of activity symmetrically positioned around the midpoint. Even though the linear analysis in Fig. 7 demonstrates three well-separated gain bands, the numerical example in Fig. 12 shows that the gain-band centered around k=5 rapidly dominates the other gain bands. This can be accounted for by the much larger positive eigenvalue (and thus growth rate) of this gain band ($\lambda \sim$ 2-3) compared to the other gain bands where the eigenvalues are less than 0.4. Thus the linearly most unstable gain band around k=5 extracts energy from the other modes, and the outcome is a stationary and roughly periodic pattern with a typical wavelength of about $2\pi/5 \sim 1.25$. A detailed analysis of the dynamical devel-

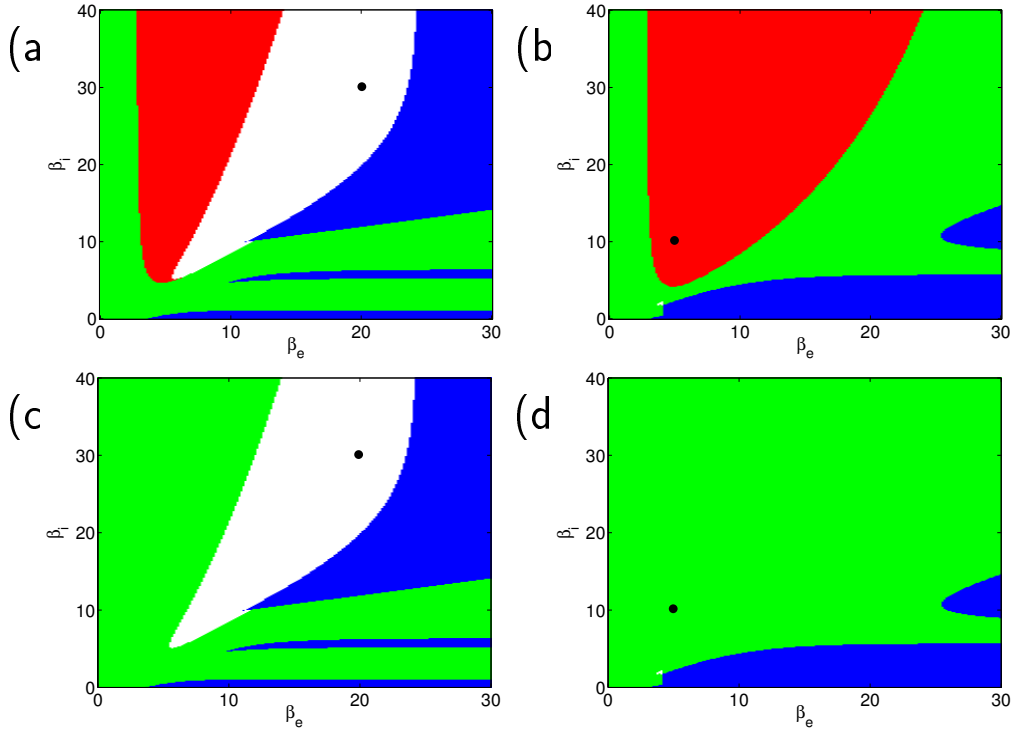


Fig. 11. Color plots illustrating pattern formation as a function of inclination parameters $(\beta_{\rm e}, \beta_{\rm i})$. Exponentially decaying connectivity functions and synaptic footprints as in Fig. 5. Unique equilibrium situations for the local problem corresponds to the white, red and green regions. White regions correspond to parameters providing stationary spatial oscillatory patterns, red regions to spatiotemporal oscillations, while no patterns are formed in green regions. The blue regions corresponds to situations with three equilibrium points in the local problem, and the patterns formed in this situation are not explored here. (a) $\theta_{\rm e} = 0.1, \theta_{\rm i} = 0.12, \tau = \tau_{\rm H} - 0.07$. Each point $(\beta_{\rm e}, \beta_{\rm i})$ corresponds to a particular value of the Hopf time $\tau_{\rm H}$ (for this particular set of parameters) determined by (8),(15) and (17). Solid dot corresponds to the values for $\beta_{\rm e}$ and $\beta_{\rm i}$ in parameter set A. (b) $\theta_{\rm e} = 0.05, \theta_{\rm i} = 0.1, \tau = \tau_{\rm H} - 0.07$. Solid dot corresponds to the values for $\beta_{\rm e}$ and $\beta_{\rm i}$ in parameter set B. (c) $\theta_{\rm e} = 0.1, \theta_{\rm i} = 0.12, \tau = 0.001$. Solid dot corresponds to the values for $\beta_{\rm e}$ and $\beta_{\rm i}$ in parameter set A. (d) $\theta_{\rm e} = 0.05, \theta_{\rm i} = 0.1, \tau = 0.001$. Solid dot corresponds to the values for $\beta_{\rm e}$ and $\beta_{\rm i}$ in parameter set B.

opment at very short times reveals signs of the other two gain bands, but we do not explore this in detail here.

8 Summary and discussion

In the present paper we have studied the Turing instability and pattern formation in a two-population neural network model. The present analysis has revealed the following general features: For all choices of the input parameters

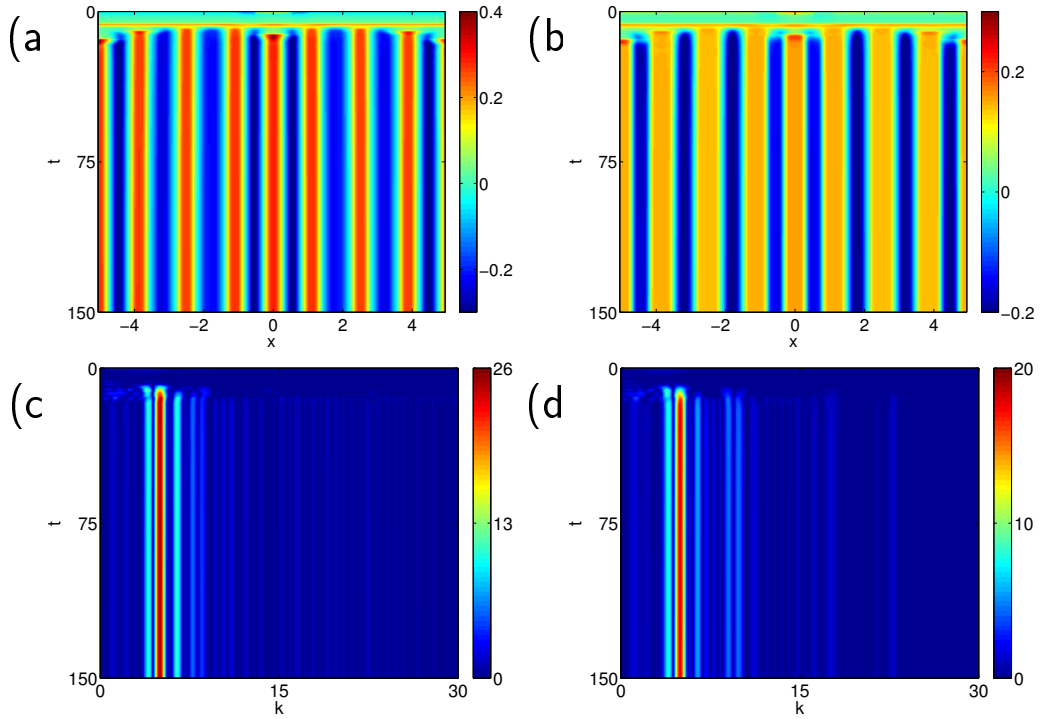


Fig. 12. Dynamical evolution of a model with rectangular-box connectivity functions (7) using the parameter set A from an initial state consisting of a homogeneous background state ($u_e = u_i = 0.129$, cf. Table 1) with a narrow centered rectangular box of neural activity superimposed ($-0.5 < x < 0.5$, $u_e = u_i = 0.2$). (a) Excitatory activity level, $u_e(x,t)$. (b) Inhibitory activity level, $u_i(x,t)$. In (c) and (d) the Fourier spectra (a) and (b), respectively, are shown.

there is at least one spatially homogeneous equilibrium point. The maximum number of equilibria for our particular sigmoidal firing-rate functions is five, while the most common multi-equilibrium scenario involves three equilibria. For positive and normalized synaptic connectivity functions which are continuous almost everywhere, the generic picture of the linear Turing instability consists of finite set of well-separated gain bands.

Two characteristic situations have been investigated in detail for models with exponentially decaying synaptic connectivity functions: (i) a single gain band found for all values of the inhibitory time constant τ, and (ii) a single gain band generated through a Turing-Hopf bifurcation as the control parameter τ increases beyond a critical value. In the first situation stationary spatial oscillations are generated; in the latter the outcome is spatiotemporal oscillations.

For our model with exponentially decaying connectivity functions, we have found that a prerequisite for having a Turing-Hopf bifurcation with the generation of spatiotemporal oscillations is that $\sigma_{ii}/\sigma_{ee} > \sqrt{(P_i'+1)P_e'/(P_i'(P_e'-1))}$ for $P_e' > 1$ (cf. (37)). Since $\sqrt{(P_i'+1)P_e'/(P_i'(P_e'-1))} > 1$ this requirement thus encompasses the requirement $\sigma_{ii} > \sigma_{ee}$ found in [18] for the Wilson-Cowan

model. For the particular firing-rate function parameters used to exemplify this situation (parameter set B, cf. Table 1) we thus find that the synaptic width of the self-inhibition of the inhibitory neurons must be at least a factor $\sqrt{(P_{\rm i}'+1)P_{\rm e}'/(P_{\rm i}'(P_{\rm e}'-1))} = 1.45$ larger than the width of the self-excitation of the excitatory neurons.

Due to the cumbersome expression for $det(\mathbf{A})$ in (30a) involving the fourth order polynomial $H_4(\eta)$ listed in Appendix B, it is difficult to derive a similarly simple condition for the generation of stationary periodic patterns. However, if we assume a simpler model where the projections from the inhibitory neurons are local, i.e., $\sigma_{\rm ii}, \sigma_{\rm ie} \to 0$, $H_4(\eta)$ is reduced to a second order polynomial in η. Simple analysis then shows that a gain band can only exist if $\sigma_{\rm ei} > \sigma_{\rm ee}$. Thus the synaptic projections from excitatory neurons to the inhibitory neurons must be spatially more extended than to the excitatory neurons. This concurs with the standard qualitative view of the requirements for localizing a solitary bump: local recurrent excitation is needed to keep the center excited while longer-range lateral inhibition is needed to prevent it from spreading out.

To further elucidate the relationship between pattern generation and the thresholds and inclinations of the firing-rate functions, we have investigated the type of instability generated (if any) for a large range of inclination parameters $\beta_{\rm e}$ and $\beta_{\rm i}$ for two sets of firing-rate threshold values $\theta_{\rm e}$ and $\theta_{\rm i}$. We observe large differences in the instability 'phase-diagram' for these two situations, demonstrating that the type of instability depends on an interplay between the parameters determining the synaptic coupling and the inclinations and thresholds of the firing-rate function. The role of the inhibitory constant τ is more transparent: it plays no role in the generation of stationary spatial oscillations, while its value is crucial in determining the possibility for spatiotemporal oscillations. For very small τ, where the model essentially is reduced to a one-population model, it was demonstrated that spatiotemporal oscillations cannot be generated; in agreement with results from [17].

To summarize, we have found that generation of spatial or, alternatively, spatiotemporal oscillations is strongly dependent on the inclinations and threshold values of the firing-rate functions and the inhibitory time constant, i.e., a particular choice of synaptic coupling function may yield both situations. The requirements on the synaptic footprints σ_{mn} $(m, n = {\rm e}, {\rm i})$, i.e., (37) for spatiotemporal oscillations, and $\sigma_{\rm ei} > \sigma_{\rm ee}$ (for the special case $\sigma_{\rm ii} = \sigma_{\rm ie} = 0$) for spatial oscillations, are additional prerequisites.

The nonlinear development of the gain bands derived in the linear stability analysis has also been investigated, demonstrating the feature of energy leakage of the modes into the linearly most unstable mode. Moreover, after a transient phase the nonlinear stage of the development is found to consist of various coherent structures, such as stationary spatial and spatiotemporal

oscillations. Further, our numerical examples implies a direct connection between the form of the linear instability and the final stationary pattern. An additional feature demonstrated in the simulations is that the stationary pattern produced for our example with the steepest firing-rate functions looks remarkably similar to the bumps derived in the Heaviside limit of the same model.

Even though our analysis of a model with rectangular synaptic connectivity functions demonstrated that a multiple gain-band structure can be obtained, the numerical computation of the non-linear development revealed that for our model example the gain-band with the largest linear growth rate rapidly dominated the other bands. Thus prominent signatures of the multiple gain bands were not seen.

Acknowledgments

JW acknowledges support from The Research Council of Norway under the grant No. 153405/432. PB was supported by the Research Council of Norway under the grant No. 160011/V30. Parts of this work were completed in 2003/04 when JW was a Visiting Fellow at Australian National University (ANU). JW wishes to thank the Australian National University for the kind hospitality during the stay. The authors will like to thank W. Królikowski, Y. Kivshar and A. Miroshnischenko (ANU), B. Ermentrout and R. Curtu (University of Pittsburgh), H.E. Plesser, A. Ponossov and K. Pettersen (Norwegian University of Life Sciences) for many fruitful and stimulating discussions during the preparation of this paper. The authors will also like to thank the reviewer for constructive remarks.

A Mathematical foundation of stability investigation

The starting point is a 2D autonomous dynamical system

$$\partial_t \underline{X} = \mathbf{A} \cdot \underline{X} \tag{A.1}$$

defined by a 2×2-matrix $\mathbf{A}$ where the real-valued elements are smooth functions of a positive continuous variable denoted by η. This situation occurs when Fourier-transforming a system of two coupled linear partial differential equations or two coupled linear integro-differential equations. The latter equations may model wave perturbations imposed on an equilibrium state. In that context the variable η is the squared modulational wave number k^2.

The eigenvalues $\lambda_\pm$ of the coefficient matrix of the system (A.1) are given as

$$\lambda_\pm = \frac{1}{2}\Big(tr(\mathbf{A}) \pm \sqrt{(tr(\mathbf{A})^2 - 4det(\mathbf{A}))}\Big) \ . \tag{A.2}$$

We introduce the following concept of stability: *If both eigenvalues have negative real part for all values of $\eta \geq 0$, the equilibrium state $\underline{X} = \underline{0}$ is said to be asymptotically stable. If at least one eigenvalue is strictly positive or the real part of both eigenvalues is strictly positive for some interval of η-values, the equilibrium state $\underline{X} = \underline{0}$ is said to be unstable.* Notice that we always have two modes in the problem corresponding to the two eigenvalues $\lambda_\pm$. The mode corresponding to λ_+ (λ_-) is referred to as the λ_+ (λ_-)-*mode*, respectively. Now, by means of standard 2D theory for autonomous systems the stability problem can conveniently be rephrased in terms of the properties of the parameterized curve

$$\underline{\gamma}(\eta) = (tr(\mathbf{A})(\eta), det(\mathbf{A})(\eta)), \quad \eta \geq 0 \tag{A.3}$$

in the 2D plane. This plane is referred to as the *invariant plane of the matrix* $\mathbf{A}$ or simply the *invariant plane*. From the stability definition we now get that the equilibrium state $\underline{X} = \underline{0}$ is asymptotically stable provided $tr(\mathbf{A}) < 0, det(\mathbf{A}) > 0$ for all values of $\eta \geq 0$, which means that the parameterized curve $\underline{\gamma}$ remains in the second quadrant of the invariant plane. Moreover, we will have instability if there is some η-interval for which the trajectory $\underline{\gamma}$ is located outside the second quadrant in the same plane. Assume $det(\mathbf{A})(\eta = 0) < 0$ or $tr(\mathbf{A})(\eta = 0) > 0$. Then by continuity the same properties hold true for some η-interval about $\eta = 0$. Hence, we can conclude that a sufficient condition for instability is either $det(\mathbf{A})(\eta = 0) < 0$ or $tr(\mathbf{A})(\eta = 0) > 0$. On the contrary, in order to have stability we must have $tr(\mathbf{A})(\eta = 0) < 0, det(\mathbf{A})(\eta = 0) > 0$. For example, we will get an instability if the trajectory $\underline{\gamma}$ starts out in the second quadrant, but leaves this quadrant by crossing the coordinate axes in the invariant plane. The generic crossing conditions are in this case expressed as either the transversal crossing condition

$$det(\mathbf{A})(\eta = \eta_1) = 0, \quad \frac{d}{d\eta}\det(\mathbf{A})(\eta = \eta_1) \neq 0, \quad tr(\mathbf{A})(\eta = \eta_1) < 0 \tag{A.4}$$

or

$$tr(\mathbf{A})(\eta = \eta_1) = 0, \quad \frac{d}{d\eta}tr(\mathbf{A})(\eta = \eta_1) \neq 0, \quad det(\mathbf{A})(\eta = \eta_1) > 0 \ . \tag{A.5}$$

In general, the instability can be classified into two categories depending on the properties of the trajectory $\underline{\gamma}$:

1. *Finite bandwidth instabilities.* We assume that we can prove that the point $(tr(\mathbf{A}), det(\mathbf{A}))$ belongs to the second quadrant of the invariant plane as $\eta \to +\infty$. Due to the continuous dependence of the coefficient matrix

on η, it is concluded that the same property holds true for η exceeding a certain threshold, say η_M. Hence in that case the instability must be of the finite bandwidth type. The generic picture consists of a union of bounded, open η-intervals for which the $\underline{\gamma}$-curve is outside the second quadrant in the invariant plane, corresponding to a numerable set of finite bands producing instabilities. The number of transversal crossings with the trace axis and the positive determinant axis determines the number of such bands. The model (2) falls into this category.

2. *Short-wavelength instabilities.* If the trajectory $\underline{\gamma}$ remains outside the second quadrant for all η exceeding a certain threshold value, we have an infinite band of η-values responsible for the instabilities. This case is referred to as a short-wavelength instability. The production of short-wavelength instabilities signals that the validity of the model under consideration breaks down, and that the model is mathematically ill-posed.

We denote the unstable bands as *gain bands*. We now investigate how the number of gain bands formed vary as a function of the number of transversal crossings with the $tr(\mathbf{A})$-axis and the positive $det(\mathbf{A})$-axis in the invariant plane. We also investigate the consequences of breakdown of nontransversal crossings of the coordinate axis. It turns out that the general stability discussion is conveniently divided into the following subcases:

A.1 Generalized Turing situation

Assume that there are strictly positive η_1, η_2 with $0 < \eta_1 < \eta_2$ such that

$$\begin{aligned} det(\mathbf{A})(\eta = \eta_i) &= 0, \\ \frac{d}{d\eta} det(\mathbf{A})(\eta = \eta_i) &\neq 0, \\ tr(\mathbf{A})(\eta = \eta_i) &< 0 \end{aligned}$$

for $i = 1, 2$. Moreover, it is assumed that the curve $\underline{\gamma}$ neither crosses the negative $tr(\mathbf{A})$ - axis nor the positive $det(\mathbf{A})$-axis transversally for $\eta_1 < \eta < \eta_2$. However, it may cross the positive $tr(\mathbf{A})$-axis. In this case we have exactly one unstable λ_+ band for $\eta_1 < \eta < \eta_2$ and N $(N = 0, 1, 2, \dots)$ unstable λ_- bands if there are $2N$ transversal crossings of the positive $tr(\mathbf{A})$ axis in the same parameter interval. Notice that this situation generalizes the classical Turing instability theory for reaction - diffusion equations.

A.2 Finite bandwidth instability with oscillations

Assume that there are strictly positive η_1, η_2 with $0 < \eta_1 < \eta_2$ such that

$$\begin{aligned} tr(\mathbf{A})(\eta = \eta_i) &= 0, \\ \frac{d}{d\eta} tr(\mathbf{A})(\eta = \eta_i) &\neq 0, \\ det(\mathbf{A})(\eta = \eta_i) &> 0 \end{aligned}$$

for $i = 1, 2$. Moreover, it is assumed that the curve $\underline{\gamma}$ neither crosses the negative $tr(\mathbf{A})$ - axis nor the positive $det(\mathbf{A})$-axis transversally for $\eta_1 < \eta < \eta_2$. However, it may cross the positive $tr(\mathbf{A})$-axis. In this case we have exactly one unstable λ_+ band for $\eta_1 < \eta < \eta_2$ and at least one unstable λ_- band. If there are $2N$ transversal crossings of the positive $tr(\mathbf{A})$-axis in the same parameter interval, the number of unstable λ_- bands is $N + 1$ ($N = 0, 1, 2, \ldots$). Due to the fact that the eigenvalues $\lambda_\pm$ appear in a complex conjugate pair for η in some neighborhood of each of the values $\eta = \eta_i; i = 1, 2$, the typical feature of this situation is a finite bandwidth instability with temporal oscillations.

A.3 Mixed Turing - finite bandwidth instability with oscillations

Assume that there are strictly positive η_1, η_2 with $0 < \eta_1 < \eta_2$ such that

$$det(\mathbf{A})(\eta = \eta_1) = 0, \quad \frac{d}{d\eta} det(\mathbf{A})(\eta = \eta_1) \neq 0, \quad tr(\mathbf{A})(\eta = \eta_1) < 0$$

$$tr(\mathbf{A})(\eta = \eta_2) = 0, \quad \frac{d}{d\eta} tr(\mathbf{A})(\eta = \eta_2) \neq 0, \quad det(\mathbf{A})(\eta = \eta_2) > 0 \ .$$

It is assumed that the curve $\underline{\gamma}$ neither crosses the negative $tr(\mathbf{A})$-axis nor the positive $det(\mathbf{A})$-axis transversally for $\eta_1 < \eta < \eta_2$. However, it may cross the positive $tr(\mathbf{A})$-axis. In this case we have exactly one unstable λ_+ band for $\eta_1 < \eta < \eta_2$ and at least one unstable λ_- band. If there are $2N - 1$ transversal crossings of the positive $tr(\mathbf{A})$-axis in the same parameter interval, the number of unstable λ_- bands is N ($N = 1, 2, \ldots$). Notice that the same argument holds true when reversing the orientation of the $\underline{\gamma}$-curve.

In general, the gain band structure may consist of the three categories elaborated in the previous subsections.

A.4 Splitting, coalescence, vanishing and formation of gain bands. Turing-Hopf bifurcation

The breakdown of the transversality conditions

$$det(\mathbf{A})(\eta = \eta_i) = \frac{d}{d\eta} det(\mathbf{A})(\eta = \eta_i) = 0 \tag{A.6}$$

or

$$tr(\mathbf{A})(\eta = \eta_i) = \frac{d}{d\eta} tr(\mathbf{A})(\eta = \eta_i) = 0 \tag{A.7}$$

for $i = 1$ or $i = 2$ signals that a splitting, coalescence, vanishing and formation of gain bands takes place. This property is to be considered as a bifurcational phenomena, i.e., the conditions can only be fulfilled for a discrete set of values of some parameter playing the role as the control parameter. In general, the non-transversal crossings are signalling the onset of instabilities, and hence interesting dynamical features. The case

$$tr(\mathbf{A})(\eta = \eta_{\mathrm{H}}) = 0, \quad \frac{d}{d\eta} tr(\mathbf{A})(\eta = \eta_{\mathrm{H}}) = 0, \quad det(\mathbf{A})(\eta = \eta_{\mathrm{H}}) > 0$$

represents the Turing-Hopf situation [20] where the result is a pair of purely imaginary eigenvalues at the bifurcation point, while the case

$$det(\mathbf{A})(\eta = \eta_T) = \frac{d}{d\eta} det(\mathbf{A})(\eta = \eta_T) = 0, \quad tr(\mathbf{A})(\eta_T) < 0$$

corresponds to the excitation of again band through a Turing-type of instability. The consequences of the Turing-Hopf bifurcation have been elaborated in detail in [20] by means of normal form theory in the context of neuronal network models. It is shown that breathers or travelling waves are excited when passing this bifurcation point. Moreover, conditions ensuring stable breathers/travelling waves are given.

Finally, notice that the stability methodology elaborated here has also been used in the study of modulational instability (MI) of plane waves in nonlocal Kerr media [32] and in quadratic $\chi^{(2)}$-materials [35]. In both these cases the wave number dependent coefficient matrix $\mathbf{A}$ is characterized by $tr(\mathbf{A}) \equiv 0$.

B Coefficients for polynomial

The coefficients of the quartic polynomial H_4 defined by (33) are given as

$$
\begin{aligned}
h_4 &= \sigma_{\rm ee}^2\sigma_{\rm ii}^2\sigma_{\rm ei}^2\sigma_{\rm ie}^2 \\
h_3 &= \sigma_{\rm ee}^2\sigma_{\rm ii}^2\sigma_{\rm ei}^2 + \sigma_{\rm ee}^2\sigma_{\rm ii}^2\sigma_{\rm ie}^2 + \sigma_{\rm ee}^2\sigma_{\rm ie}^2\sigma_{\rm ei}^2 + \sigma_{\rm ie}^2\sigma_{\rm ei}^2\sigma_{\rm ii}^2 + (P_{\rm i}'\sigma_{\rm ee}^2 - P_{\rm e}'\sigma_{\rm ii}^2)\sigma_{\rm ie}^2\sigma_{\rm ei}^2 \\
h_2 &= \sigma_{\rm ee}^2\sigma_{\rm ii}^2 + \sigma_{\rm ee}^2\sigma_{\rm ei}^2 + \sigma_{\rm ee}^2\sigma_{\rm ie}^2 + \sigma_{\rm ii}^2\sigma_{\rm ie}^2 + \sigma_{\rm ii}^2\sigma_{\rm ei}^2 + F'(u_{\rm eq})\sigma_{\rm ei}^2\sigma_{\rm ie}^2 \\
&\quad + (P_{\rm i}'\sigma_{\rm ee}^2 - P_{\rm e}'\sigma_{\rm ii}^2)(\sigma_{\rm ie}^2 + \sigma_{\rm ei}^2) + P_{\rm e}'P_{\rm i}'(\sigma_{\rm ee}^2\sigma_{\rm ii}^2 - \sigma_{\rm ei}^2\sigma_{\rm ie}^2) \\
h_1 &= (1 + P_{\rm e}'P_{\rm i}')(\sigma_{\rm ee}^2 + \sigma_{\rm ii}^2) + (F'(u_{\rm eq}) - P_{\rm e}'P_{\rm i}')(\sigma_{\rm ei}^2 + \sigma_{\rm ie}^2) + P_{\rm i}'\sigma_{\rm ee}^2 - P_{\rm e}'\sigma_{\rm ii}^2 \\
h_0 &= F'(u_{\rm eq})\ .
\end{aligned}
$$

References

[1] P.Dayan, L.F. Abbott, Theoretical neuroscience, MIT Press, Cambridge, MA, 2001.

[2] T.P. Vogels, K. Rajan, L.F. Abbott, Neural network dynamics, Ann. Rev. Neurosci. 28 (2005) 357–376.

[3] S. Amari, Dynamics of pattern formation in lateral-inhibition type neural fields, Biological Cybernetics 27 (1977) 77–87.

[4] D.J. Pinto, G.B. Ermentrout, Spatially structured activity in synaptically coupled neuronal networks: II. Lateral inhibition and standing pulses, SIAM J. Appl. Math. 62 (2001) 226–243.

[5] C.R. Laing, W.C. Troy, B. Gutkin, G.B. Ermentrout, Multiple bumps in a neuronal network model of working memory, SIAM J. Appl. Math. 63 (2002) 62–97.

[6] C.R. Laing and W.C. Troy, Two-bump solutions af Amari- type models of neuronal pattern formation, Physica D 178 (2003) 90–218.

[7] S. Coombes, G.J. Lord, M.R. Owen, Waves and bumps in neuronal networks with axo-dendritic synaptic interactions, Physica D 178 (2003) 219–241.

[8] J.E. Rubin, W.C. Troy, Sustained spatial patterns of activity in neuronal populations without recurrent excitation, SIAM J. Appl. Math. 64 (2004) 1609–1635.

[9] S.E. Folias, P.C. Bressloff, Breathing pulses in an excitatory network, SIAM J. Appl. Dyn. Syst. 3 (2004) 378–407.

[10] S. Coombes, M.R. Owen, Bumps, breathers, and waves in a neural network with spike frequency adaptation, Phys. Rev. Lett. (2005) 148102.

[11] Y. Guo, C.C. Chow, Existence and stability of standing pulses in neural networks: I. Existence, SIAM J. Appl. Dyn. Sys. 4 (2005) 217–248.

[12] Y. Guo, C.C. Chow, Existence and stability of standing pulses in neural networks: II. Stability, SIAM J. Appl. Dyn. Sys. 4 (2005) 249–281.

[13] P. Blomquist, J. Wyller, G.T. Einevoll, Localized activity patterns in two-population neuronal network, Physica D 206 (2005) 180–212.

[14] G.B. Ermentrout, J.D. Cowan, Large scale spatially organized activity in neural nets, SIAM J. Appl. Math. 38 (1980) 1–21.

[15] A. Hutt, M. Bestehorn, T. Wennekers, Pattern formation in intracortical neuronal fields, Network: Comp. Neur. Syst. 14 (2003) 351–368.

[16] A. Hutt, F.M. Atay, Analysis of nonlocal neural fields for both general and gamma-distributed connectivities, Physica D 203 (2005) 30–54.

[17] F.M. Atay, A. Hutt, Stability and bifurcations in neural fields with finite propagation speed and general connectivity, SIAM J. Appl. Math. 65 (2005) 644–666.

[18] G.B. Ermentrout, J.D. Cowan, Temporal oscillations in neuronal nets, J. Math. Biology 7 (1979) 265–280.

[19] G.B. Ermentrout, J.D. Cowan, Secondary bifurcations in neuronal nets, SIAM J. Appl. Math. 39 (1980) 323–340.

[20] R. Curtu, B. Ermentrout, Pattern formation in a network of excitatory and inhibitory cells with adaptation, SIAM J. Applied Dynamical Systems 3(2004) 191–231.

[21] C. Laing, S. Coombes, The importance of different timings of excitatory and inhibitory pathways in neural field models, Network: Computation in Neural Systems 17 (2006) 151–172.

[22] M.A.P. Idiart, L.F. Abbott, Propagation of excitation in neural networks, Network 4 (1993) 285–294.

[23] D.J. Pinto, G.B. Ermentrout, Spatially structured activity in synaptically coupled neuronal networks: I. Traveling fronts and pulses, SIAM J. Appl. Math. 62 (2001), 206-225.

[24] P.C. Bressloff, S.E. Folias, Front bifurcations in an excitatory neural network, SIAM J. Appl. Math. 65 (2004) 131–151.

[25] S. Coombes, M.R. Owen, Evans functions for integral neural field equations with Heaviside firing rate functions, SIAM J. Appl. Dyn. Sys. 3 (2004) 574–600.

[26] D.J. Pinto, R.K. Jackson, C.E. Wayne, Existence and stability of traveling pulses in a continuous neuronal network, SIAM J. Appl. Dyn. Sys. 4 (2005) 954–984.

[27] H.R. Wilson and J.D. Cowan, A mathematical theory of the functional dynamics of cortical and thalamic nervous tissue, Kybernetik 13 (1973), pp. 55–80.

[28] B. Ermentrout, Neural networks as spatio-temporal pattern-forming systems, Rep. Prog. Phys. 61 (1998), pp. 353–430.

[29] S. Coombes, Waves, bumps, and patterns in neural field theories, Biol. Cybern. 93 (2005), pp. 91–108.

[30] G.B. Ermentrout, A mathematical theory of visual hallucination patterns, Biol. Cybern 34 (1979) 137–150.

[31] J.D. Murray, Mathematical biology, Springer-Verlag, New York, NY, 1989, Ch. 16.

[32] J. Wyller, W. Królikowski, O. Bang and J.J. Rasmussen, Generic features of modulational instability in nonlocal Kerr media, Phys. Rev. E, 66 (2002), 066615.

[33] B. Ermentrout, Simulating, analyzing, and animating dynamical systems: A guide to XPPAUT to researchers and students, SIAM, Philadelphia, PA, 2002.

[34] L. Perko, Differential Equations and Dynamical Systems, 3. ed. Texts in Applied Mathematics Vol. 7, Springer-Verlag, New York, NY, 2000.

[35] J. Wyller, W. Królikowski, O. Bang, D. E. Petersen and J.J. Rasmussen, Modulational instability in the nonlocal $\chi^{(2)}$ - model, submitted, 2006.